Wave propagation in Prestressed Structures with Geometric Nonlinearities through Carrera Unified Formulation

Wave Propagation in Prestressed Structures with Geometric Nonlinearities through Carrera Unified Formulation *

Matteo Filippi[†a], Dario Magliacano[‡a], Marco Petrolo[§a], and Erasmo Carrera[¶a]
[a]*Polytechnic of Turin*
Corso Duca degli Abruzzi 24, 10129 Turin, Italy

This paper deals with the analysis of wave propagation characteristics in various prestressed structures with geometric nonlinearities using the Carrera Unified Formulation (CUF). CUF provides a versatile platform to model a wide range of structures and nonlinearities that can take care of all wave propagation aspects. In this work, different geometric nonlinearities, for which representative governing equations have been derived and numerical solutions have been obtained through a unified approach, are considered. The study investigates in detail the effect of prestress and geometric nonlinearity on wave propagation behavior. The results indicate that prestress has a very influential effect on modal frequency and dispersion characteristics for wave propagation. Specifically, three CUF-modeled beams are considered herein, having a sandwich, metallic portal and metallic box cross-section, respectively. Initially, the principal cross-sectional modal shapes of the unstressed, linear, and full nonlinear (i.e., full 3D Green-Lagrange strains matrix) beam with a prestress are investigated, among which torsional and flexural modes can be recognized. Afterward, the equilibrium curves of such structures for various geometrical nonlinear approximations are traced, highlighting that most types of nonlinearity induce a hardening behavior in the system, which increases with the preload, directly leading to a variation in modal frequencies. The dispersion relations of the full nonlinear structure examined as a function of the applied preload are further compared, enriching the investigation by exploiting Wave Finite Element Method capabilities. This knowledge paves the way toward the design and optimization of prestressed systems with enhanced acoustic performance and that fosters the development of sound absorption, noise insulation, and structural isolation.

*The present research represents an extension of the conference paper "Filippi M., Magliacano D., Petrolo M., and Carrera E., Wave Propagation in Pre-stressed Structures with Geometric Non-linearities through Carrera Unified Formulation, 30th AIAA/CEAS Aeroacoustics Conference, 04/06/2024-07/06/2024, Rome (Italy), AIAA Paper Number: 2024-4054558, DOI: 10.2514/6.2024-3028".

[†]Assistant Professor, Department of Mechanical and Aerospace Engineering
[‡]Assistant Professor, Department of Mechanical and Aerospace Engineering, dario.magliacano@polito.it
[§]Associate Professor, Department of Mechanical and Aerospace Engineering
[¶]Full Professor, Department of Mechanical and Aerospace Engineering

I. Introduction

A. Background and Motivation

The present research represents an extension of its homonym conference paper from the same authors [1]. In the field of acoustics, understanding the wave propagation characteristics of structures is crucial for assessing their ability to transmit or suppress sound waves. Due to their inherent internal stresses and unique material properties, prestressed structures exhibit distinct wave propagation behavior that has not been extensively investigated yet. Traditionally [2], the wave propagation analysis in prestressed structures has relied on simplified models that neglect geometric nonlinearities. However, these simplifications may lead to inaccurate predictions, especially in cases where large deformations or initial curvature are present. The Carrera Unified Formulation (CUF) [3] emerges as a powerful tool to address this limitation, offering a versatile framework for modeling various structural configurations (such as for reinforced aircraft shells [4] and composite beams [5]) and nonlinearity types (such as refined beam [6] and shell [7] theories), enabling a comprehensive analysis of wave propagation phenomena and taking into account several kinematics [8]. The motivation for this study stems from the need for a thorough understanding of wave propagation behavior in prestressed structures with different geometric nonlinearities. This understanding is essential for designing and analyzing prestressed structures with enhanced acoustic performance, such as sound-absorbing panels, noise barriers, and acoustic-structural meta-materials [9, 10]. In the latter field, Magliacano *et al.* investigated different approaches based on active [11] and passive [12–15] noise control techniques. In this context, Casaburo *et al.* [16] aimed at the optimization of the acoustic properties of a meta-material using machine learning techniques, while Catapane *et al.* focused on tunable tonal resonators, such as those based on Helmholtz [17] and labyrinth [18] principles. By elucidating the effects of prestress and geometric nonlinearity on wave propagation, this study aims to advance acoustic engineering and design structures with improved acoustic properties.

B. Literature Review

The study of wave propagation in prestressed structures has gained significant attention in recent years; numerous studies have investigated the effects of prestress on wave propagation characteristics, mostly focusing on the linear regime. However, geometric nonlinearities, often encountered in prestressed structures, have not yet been extensively studied in the context of wave propagation.

Several researchers have employed simplified models to analyze wave propagation in prestressed structures with geometric nonlinearities. For instance, Gei *et al.* [19] addressed the issue of the so-called effective negative mass effect for frequencies within the stop bands of an unperturbed structure, proposing a constructive algorithm of controlling the stop bands and hence filtering properties and resonance, also investigating the band structure of dispersion diagrams for axial and flexural waves of quasi-periodic infinite beams [20]. Parnell [21] studied viscoelastic wave propagation along prestressed nonlinear elastic composite bars, deriving explicit forms for the effective incremental storage and loss

moduli with dependence on the prestress. Barnwell *et al.* [22] found that prestress significantly affects the band-gap structure for Mooney-Rivlin and Fung-type materials, allowing stop bands to be switched on and off; in their studies, it is also shown that for a specific class of materials, the phononic properties remain invariant under nonlinear deformation, permitting some particular behaviors and leading to the possibility of phononic cloaks. Subsequently, the same authors [23] investigated the effect of nonlinear elastic prestress on coupled compressional and vertically polarized shear elastic wave propagation in a two-dimensional periodic structure. Zhang *et al.* [24] further investigated the effect of the applied preload on wave propagating behaviors of hexagonal lattices in terms of band structures, band gap distributions, and phase/group velocities, devoting special attention to the effect of preload on the directional energy flow. De Pascalis *et al.* [25] employed genetic algorithms to theoretically design a range of phononic media that can act to prevent or ensure anti-plane elastic wave propagation over a specific range of low frequencies, with each case corresponding to a particular prestress level.

More recently, researchers have begun to explore using more sophisticated models, such as the Carrera Unified Formulation (CUF) [26, 27], to analyze wave propagation in prestressed structures with geometric nonlinearities. For example, Cabral *et al.* [28] dealt with the buckling load prediction of reinforced laminated composite panels of aeronautical interest, utilizing the vibration correlation technique (VCT) as a nondestructive means to extrapolate critical loads from free vibration measurements. Wu *et al.* [29] developed a unified formulation of a full geometrically nonlinear refined plate theory in a total Lagrangian approach to investigate the large-deflection and post-buckling response of isotropic rectangular plates. Pagani and Carrera [30] confirmed the capabilities of this methodology when dealing with large displacements and post-buckling response also in the case of composite laminated beams. Filippi *et al.* [31] introduced advanced kinematics plate and shell models to evaluate the dispersion characteristics of two-dimensional waveguides, utilizing high-order functions to interpolate primary variables both in thickness and cross-section.

Prestressed structures offer unique acoustic properties that make them suitable for various applications. The presence of prestress can modify the wave propagation characteristics of these structures, leading to enhanced sound absorption and improved noise insulation.

- Sound Absorption: Prestressed structures can be designed to effectively absorb sound waves, making them suitable for noise reduction and room acoustics applications. The internal stresses in prestressed structures can introduce additional damping mechanisms that dissipate acoustic energy, leading to reduced sound levels.
- Noise Insulation: Prestressed structures can be employed as noise barriers to block or attenuate unwanted sound transmission. Their unique wave propagation characteristics can help to reduce the transmission of sound waves from one side of the structure to the other.

Despite these developments, there is still a real scarcity of detailed investigations concerning the individual and combined effects of prestress and geometric nonlinearity on wave propagation characteristics in prestressed structures. In this regard, the present study contributes a detailed analysis on the phenomenon of wave propagation in prestressed

structures with different geometric nonlinearities using CUF.

C. Research Objectives

The primary objective of this study is to investigate the wave propagation characteristics in prestressed structures with different geometric nonlinearities utilizing the Carrera Unified Formulation (CUF) and focusing on a sandwich beam, a metallic portal beam and a metallic box beam, whose dynamic linear characteristics have been analyzed by Filippi *et al.* [32]. In Section II, the theoretical framework about CUF, geometric nonlinearities and prestress modeling is outlined, and the governing equations for wave propagation in prestressed structures with different geometric nonlinearities are derived using CUF; in Section III, the effects of prestress and geometric nonlinearity on wave propagation characteristics are systematically investigated, thus providing valuable insights into the wave propagation phenomena in prestressed structures with different geometric nonlinearities and contributing to the understanding of wave propagation in complex structural systems; Section IV summarizes the obtained results and foresees some possible future perspectives in this topic. The objectives of this study are, upon achievement, likely to give an all-rounded understanding of wave propagation in prestressed structures with different geometric nonlinearities.

This research is further extended to the study of dispersion relations of a full nonlinear structure with the application of different levels of preload using WFEM. It is one of the techniques that can provide full characterization of wave propagation in a mechanical loading state. The dispersion relation, as a function of changes of wavenumber with frequency, conveys very useful information on the wave propagation behavior within the waveguide. The dispersion curves under various preloads can give insights into how the mechanical loading affects wave propagation in the waveguide. The information is critical in the design of waveguides that should transmit or confine waves for a particular application. All in all, such understanding may have essential implications for the waveguide design and analysis under static loads.

II. Theoretical Framework

A. Carrera Unified Formulation (CUF)

The Carrera unified formulation is a very strong and flexible tool for the modeling of various structural configurations, such as beams, plates, and shells. Quite different from the classic methods based on a layer-wise or equivalent single layer approach, CUF employs a unique framework wherein the displacement field is expressed by a series of expansion functions. This approach offers several advantages, including:

- High-order accuracy: CUF can achieve high-order accuracy by using more expansion functions, enabling the capture of complex strain and displacement fields.
- Geometric flexibility: CUF can accommodate various structural configurations, including beams with variable cross-sections, plates with arbitrary shapes, and shells with different geometries.

- Nonlinearity modeling: CUF can incorporate various nonlinearity types, such as geometric nonlinearities (large deformations, initial curvature) and material nonlinearities (nonlinear constitutive laws).
- Computational efficiency: CUF can achieve computational efficiency using appropriate expansion functions and numerical techniques.

In the framework of the Carrera Unified Formulation, the 3D displacement field $\mathbf{u}(x, y, z)$ is written as a general expansion of the primary unknowns that, in the case of a beam, is reported in Eq. (1):

$$\mathbf{u}(x, y, z) = F_\tau(x, z)\mathbf{u}_\tau(y), \tau = 0, 1, ..., N \tag{1}$$

in which F_τ represents a set of cross-section expansion functions, $\mathbf{u}_\tau$ indicates the generalized displacement vector depending on the y coordinate, N is the order of expansion in the thickness direction and the repeated index τ denotes summation. The expansion functions can be chosen based on the specific requirements of the problem. For example, Legendre polynomials are commonly used for beams and plates. In contrast, shells often employ higher-order expansion functions, such as Legendre-Lagrange or Hermite polynomials, to capture complex geometries and nonlinearity. In the present work, Lagrange polynomials [6], from now on indicated by "LE", are assumed for the expansion functions F_τ; in this case, the unknown variables are pure displacements. According to the finite element method (FEM), the generalized displacement vector $\mathbf{u}_\tau$ is approximated based on the finite element (FE) nodal parameters $\mathbf{q}_{\tau i}$ and shape functions N_i as reported in Eq. (2) [33]:

$$\mathbf{u}_\tau(y) = N_i(y)\mathbf{q}_{\tau i}, i = 1, 2, ..., n_{el} \tag{2}$$

in which N_i are the i^{th} shape functions, $\mathbf{q}_{\tau i}$ represents the unknown nodal variables, n_{el} is the number of nodes per element and i indicates summation [34]. This article employs 2D nine-node quadratic FEs for the shape functions in the $x - z$ plane. A system of differential equations is obtained by substituting the expansion functions into the governing equation and applying the principle of virtual work.

B. Geometric Nonlinearities

Geometric nonlinearities arise when a structure's deformations are sufficiently large that the initial geometry significantly affects the structural response. This can occur in various situations, such as:

- Large deflections: When a structure undergoes large deflections, the initial geometry no longer accurately represents the deformed shape. This can lead to changes in stiffness, buckling behavior, and wave propagation characteristics.
- Initial curvature: Structures with inherent curvatures, such as prestressed beams or curved shells, exhibit geometric nonlinearities due to the non-zero initial strains and stresses. This can influence wave propagation behavior and

lead to wave trapping and mode conversion phenomena.

- Contact interactions: The geometric relationships between the contacting surfaces must be considered when structures undergo contact interactions. This can introduce nonlinearities into the system and affect wave propagation characteristics.

CUF can effectively model various geometric nonlinearities by incorporating the deformed geometry into the expansion functions. This allows CUF to capture the effects of geometric nonlinearity on the structural response, including wave propagation behavior.

In the context of wave propagation, geometric nonlinearities can lead to several complex phenomena, such as:

- Wave trapping: Geometric nonlinearities can trap waves within specific structure regions, preventing their propagation through the entire structure.
- Mode conversion: Geometric nonlinearities can cause the transformation of one wave mode into another, leading to a change in the wave characteristics.
- Wave localization: Geometric nonlinearities can localize waves at specific locations within the structure, resulting in a wave energy concentration.

A compact form of the displacement–strain relations is reported in Carrera *et al.* [35]. Hooke's law expresses the relation between $\boldsymbol{\sigma}$ and $\boldsymbol{\epsilon}$ for a linear elastic isotropic metallic material as $\boldsymbol{\sigma} = \mathbf{C}\boldsymbol{\epsilon}$, where $\mathbf{C}$ is the material matrix. Understanding the effects of geometric nonlinearities on wave propagation is crucial for designing prestressed structures that can withstand static loads and ensure their safety and reliability.

C. Prestress Modeling

Prestress can significantly influence wave characteristics in wave propagation, including wave velocity, attenuation, and dispersion properties. Prestress introduces additional stiffness into the structure, which can alter the wave propagation behavior. Moreover, prestress can induce initial strains and stresses, further modifying wave propagation.

- Wave Velocity: Prestress generally increases the wave velocity in prestressed structures. This is because the additional stiffness introduced by prestress increases the structure's resistance to deformation, leading to faster wave propagation. The increase in wave velocity is more pronounced for higher prestress levels.
- Attenuation: Prestress can also affect the attenuation of waves in prestressed structures. Attenuation is the reduction in wave amplitude as it propagates through the structure. Prestress can increase or decrease attenuation depending on the specific conditions. Prestress can sometimes introduce additional damping mechanisms that lead to increased attenuation. Prestress can alter the wave propagation path in other cases, leading to decreased attenuation.
- Dispersion: Prestress can also influence the dispersion of waves in prestressed structures. Dispersion is the phenomenon where waves of different frequencies propagate at different velocities. Prestress can modify the

dispersion characteristics of waves, leading to changes in the wave group velocity and spreading rate.

Specific effects of prestress on wave propagation relate to a lot of factors, such as the level of prestress, type of structural element, or even wave propagation mode. The effects of prestress on wave propagation need to be well understood to allow for the design of prestressed structures that can resist static loads and ensure safety and reliability. CUF models prestress effectively by considering the initial stress state in the governing equations. In this way, CUF manages to capture the effects of initial prestress on the structural response related to wave propagation.

Clearly, the method to include prestress in CUF depends on the type of structural element and the prestressing technique used. For prestressed beams, one simplification that is often used is to model the prestress force as an external force applied at the locations of the prestressing tendons. In prestressed shells, it is possible to include the prestress stress field directly into the expansion functions. Long-term prestress wave propagation behavior can be fully understood with CUF due to its capability for accurate modeling, which is the basis for the design of systems optimized for dynamic performance and safety.

D. Governing Equations

CUF is based on the principle of virtual work, where the sum of the external forces that perform work corresponding to a virtual displacement is equal to the sum of all the internal forces performing work for the same virtual displacement. In the case of geometric nonlinearities, one must use an updated Lagrangian formulation that takes into account the deformed geometry of the structure. The virtual variation of internal strain energy is calculated as reported in Eq. (3):

$$\delta L_{int} =< \delta \boldsymbol{\epsilon}^{\mathrm{T}} \boldsymbol{\sigma} > \tag{3}$$

in which $< (\cdot) >= \int_V (\cdot) dV$, where V represents the initial undeformed volume of the structure considering the hypothesis of small deformations, and δ is the virtual variation operator. It is proved that [34]:

$$\begin{aligned} \delta L_{\text{int}} &= \delta \mathbf{q}_{sj}^{\mathrm{T}} < \left(\mathbf{B}_l^{sj} + 2\mathbf{B}_{nl}^{sj} \right)^{\mathrm{T}} \mathbf{C} \left(\mathbf{B}_l^{\tau i} + \mathbf{B}_{nl}^{\tau i} \right) > \mathbf{q}_{\tau i} \\ &= \delta \mathbf{q}_{sj}^{\mathrm{T}} \mathbf{K}_0^{jis\tau} \mathbf{q}_{\tau i} + \delta \mathbf{q}_{sj}^{\mathrm{T}} \mathbf{K}_{lnl}^{jis\tau} \mathbf{q}_{\tau i} + \delta \mathbf{q}_{sj}^{\mathrm{T}} \mathbf{K}_{nll}^{jis\tau} \mathbf{q}_{\tau i} + \delta \mathbf{q}_{sj}^{\mathrm{T}} \mathbf{K}_{nlnl}^{jis\tau} \mathbf{q}_{\tau i} \\ &= \delta \mathbf{q}_{sj}^{\mathrm{T}} \mathbf{K}_S^{jis\tau} \mathbf{q}_{\tau i} \end{aligned} \tag{4}$$

In Eq. (4), the two matrices $\mathbf{B}_l$ and $\mathbf{B}_{nl}$ are the linear and nonlinear geometrical matrices, respectively, whose complete form is given in Eq. (5) [35], while $\mathbf{K}_S^{jis\tau} = \mathbf{K}_0^{jis\tau} + \mathbf{K}_{lnl}^{jis\tau} + \mathbf{K}_{nll}^{jis\tau} + \mathbf{K}_{nlnl}^{jis\tau}$ represents the fundamental nuclei of the secant stiffness matrix.

$$\mathbf{B}_l = \begin{bmatrix} \partial_x & 0 & 0 \\ 0 & \partial_y & 0 \\ 0 & 0 & \partial_z \\ \partial_z & 0 & \partial_x \\ 0 & \partial_z & \partial_y \\ \partial_y & \partial_x & 0 \end{bmatrix}, \quad \mathbf{B}_{nl} = \begin{bmatrix} \frac{1}{2}(\partial_x)^2 & \frac{1}{2}(\partial_x)^2 & \frac{1}{2}(\partial_x)^2 \\ \frac{1}{2}(\partial_y)^2 & \frac{1}{2}(\partial_y)^2 & \frac{1}{2}(\partial_y)^2 \\ \frac{1}{2}(\partial_z)^2 & \frac{1}{2}(\partial_z)^2 & \frac{1}{2}(\partial_z)^2 \\ \partial_x\partial_z & \partial_x\partial_z & \partial_x\partial_z \\ \partial_y\partial_z & \partial_y\partial_z & \partial_y\partial_z \\ \partial_x\partial_y & \partial_x\partial_y & \partial_x\partial_y \end{bmatrix} \tag{5}$$

In the case of conservative loading, the tangent stiffness matrix is obtained by linearizing the virtual variation of the internal strain energy, which is expressed as reported in Eq. (6):

$$\delta\left(\delta L_{\text{int}}\right) = < \delta\left(\delta\boldsymbol{\epsilon}^{\mathrm{T}}\boldsymbol{\sigma}\right) > = < \delta\boldsymbol{\epsilon}^{\mathrm{T}}\delta\boldsymbol{\sigma} > + < \delta\left(\delta\boldsymbol{\epsilon}^{\mathrm{T}}\right)\boldsymbol{\sigma} > = \delta\mathbf{q}_{sj}^{\mathrm{T}}\mathbf{K}_T^{jis\tau}\delta\mathbf{q}_{\tau i} \tag{6}$$

where $\mathbf{K}_T^{jis\tau} = \mathbf{K}_0^{jis\tau} + \mathbf{K}_{T_1}^{jis\tau} + \mathbf{K}_\sigma^{jis\tau}$. The first term $< \delta\boldsymbol{\epsilon}^{\mathrm{T}}\delta\boldsymbol{\sigma} >$ in Eq. (6) requires the constitutive equation to be linearized, thus leading to Eqs. (7) and (8):

$$\delta\boldsymbol{\sigma} = \delta(\mathbf{C}\epsilon) = \mathbf{C}\delta\boldsymbol{\epsilon} = \mathbf{C}\left(\mathbf{B}_l^{\tau i} + 2\mathbf{B}_{nl}^{\tau i}\right)\delta\mathbf{q}_{\tau i} \tag{7}$$

$$\begin{aligned} < \delta\boldsymbol{\epsilon}^{\mathrm{T}}\delta\boldsymbol{\sigma} > &= \delta\mathbf{q}_{sj}^{\mathrm{T}} < \left(\mathbf{B}_l^{sj} + 2\mathbf{B}_{nl}^{sj}\right)^{\mathrm{T}}\mathbf{C}\left(\mathbf{B}_l^{\tau i} + 2\mathbf{B}_{nl}^{\tau i}\right) > \delta\mathbf{q}_{\tau i} \\ &= \delta\mathbf{q}_{sj}^{\mathrm{T}}\mathbf{K}_0^{jis\tau}\delta\mathbf{q}_{\tau i} + \delta\mathbf{q}_{sj}^{\mathrm{T}}\left(2\mathbf{K}_{lnl}^{jis\tau}\right)\delta\mathbf{q}_{\tau i} + \delta\mathbf{q}_{sj}^{\mathrm{T}}\mathbf{K}_{nll}^{jis\tau}\delta\mathbf{q}_{\tau i} + \delta\mathbf{q}_{sj}^{\mathrm{T}}\left(2\mathbf{K}_{nlnl}^{jis\tau}\right)\delta\mathbf{q}_{\tau i} \\ &= \delta\mathbf{q}_{sj}^{\mathrm{T}}\left(\mathbf{K}_0^{jis\tau} + \mathbf{K}_{T_1}^{jis\tau}\right)\delta\mathbf{q}_{\tau i} \end{aligned} \tag{8}$$

where $\mathbf{K}_{T_1}^{jis\tau} = 2\mathbf{K}_{lnl}^{jis\tau} + \mathbf{K}_{nll}^{jis\tau} + 2\mathbf{K}_{nlnl}^{jis\tau}$ represents the nonlinear contribution of the fundamental nuclei of the tangent stiffness matrix resulting from the linearization of the constitutive relation. The evaluation of the second term $< \delta\left(\delta\boldsymbol{\epsilon}^{\mathrm{T}}\right)\boldsymbol{\sigma} >$ in Eq. (6) requires linearizing the nonlinear geometrical relations, as further detailed by Carrera *et al.* [34].

These are the governing equations for wave propagation in structures with geometric nonlinearities using the Carrera Unified Formulation, which can be solved using various numerical techniques, such as FEM, to obtain the displacement and stress fields throughout the structure.

E. Wave Finite Element Method

By leveraging the indicial CUF formalism, the governing equations of motion for waveguide segments can be readily obtained, regardless of the specific kinematic field being considered, as

$$\left(\mathbf{K} + j\omega\mathbf{C} - \omega^2\mathbf{M}\right)\mathbf{q} = \mathbf{F} \Rightarrow \mathbf{D}(\omega)\mathbf{q} = \mathbf{F} \tag{9}$$

where $\mathbf{K}$, $\mathbf{C}$, and $\mathbf{M}$ are, respectively, the stiffness, damping, and mass matrices, $\mathbf{F}$ is the vector of the nodal forces, and $\mathbf{q}$ is the vector of the degrees of freedom. The motion of the waveguide segment is governed by the dynamic stiffness matrix $\mathbf{D} = \left(\mathbf{K} + j\omega\mathbf{C} - \omega^2\mathbf{M}\right)$. Eq. 9 describes the dynamic behavior of the waveguide segment under harmonic excitation, where both forces and displacements vary sinusoidally with time. The subscripts (L), (R), and (I) denote the left, right, and interior nodes of the one-dimensional finite element model, respectively. This notation allows to associate each term of the matrices and vectors in Eq. 9 with specific nodes in the FE model:

$$\begin{pmatrix} \mathbf{D}_{LL} & \mathbf{D}_{LI} & \mathbf{D}_{LR} \\ \mathbf{D}_{IL} & \mathbf{D}_{II} & \mathbf{D}_{IR} \\ \mathbf{D}_{RL} & \mathbf{D}_{RI} & \mathbf{D}_{RR} \end{pmatrix} \begin{pmatrix} \mathbf{q}_L \\ \mathbf{q}_I \\ \mathbf{q}_R \end{pmatrix} = \begin{pmatrix} \mathbf{F}_L \\ \mathbf{F}_I \\ \mathbf{F}_R \end{pmatrix} \tag{10}$$

If $\mathbf{F}_I = 0$, the system dimension can be reduced by expressing the interior degrees of freedom $\mathbf{q}_I$ in terms of $\mathbf{q}_L$ and $\mathbf{q}_R$. Thus, Eq. 10 can be written as reported in Eq. 11:

$$\begin{pmatrix} \mathbf{D}_{LL} & \mathbf{D}_{LR} \\ \mathbf{D}_{RL} & \mathbf{D}_{RR} \end{pmatrix} \begin{pmatrix} \mathbf{q}_L \\ \mathbf{q}_R \end{pmatrix} = \begin{pmatrix} \mathbf{F}_L \\ \mathbf{F}_R \end{pmatrix} \tag{11}$$

According to Bloch's theorem, the relation between the displacements and forces at the left and right sides of the periodic structure is

$$\begin{pmatrix} \mathbf{q}_R \\ \mathbf{F}_R \end{pmatrix} = \lambda_y \begin{pmatrix} \mathbf{q}_L \\ -\mathbf{F}_L \end{pmatrix} \quad \text{with} \quad \lambda_y = e^{-j\cdot k\cdot \Delta} \tag{12}$$

where the wavenumber is denoted by k, and the product $(-j \cdot k \cdot \Delta)$ represents the complex propagation constant. Bloch's theorem was chosen owing to the goal of studying the behavior of waves under periodic conditions. This allows numerical modeling of an infinitely long waveguide, which is much more computationally effective and sufficient for the purpose of wave dispersion study, even in the case of longitudinally homogeneous structures. As a consequence of this approach, dispersion phenomena do not depend on the chosen waveguide portion length, thus allowing to obtain generalized results. The periodic and equilibrium conditions for displacements and forces between two adjacent waveguide sections (referred to as $s1$ and $s2$) are as follows:

$$\begin{pmatrix} \mathbf{q}_R^{s1} \\ \mathbf{F}_R^{s1} \end{pmatrix} = \begin{pmatrix} \mathbf{q}_L^{s2} \\ -\mathbf{F}_L^{s2} \end{pmatrix} \tag{13}$$

By using Eqs. 11, 12, and 13, the dispersion problem becomes

$$\mathbf{T}\begin{pmatrix} \mathbf{q}_L \\ -\mathbf{F}_L \end{pmatrix} = \lambda_y \begin{pmatrix} \mathbf{q}_L \\ -\mathbf{F}_L \end{pmatrix}; \mathbf{T} = \begin{pmatrix} -\mathbf{D}_{LR}^{-1}\mathbf{D}_{LL} & \mathbf{D}_{RL}^{-1} \\ -\mathbf{D}_{RL} + \mathbf{D}_{RR}\mathbf{D}_{LR}^{-1}\mathbf{D}_{LL} & -\mathbf{D}_{RR}\mathbf{D}_{LR}^{-1} \end{pmatrix} \tag{14}$$

where $\mathbf{T}$ is the transfer matrix. Eq. 14 is solved for a range of propagation frequencies to determine the eigenvalues λ_y, which represent the wavenumbers associated with each frequency. Real eigenvalues correspond to propagating waves that can travel along the waveguide, while imaginary eigenvalues indicate evanescent waves that decay over distance. Complex eigenvalues signify attenuating waves that lose energy as they propagate. The eigenvectors obtained from solving Eq. 14 contain coefficients that are used to reconstruct the kinematic field of the waveguide. These coefficients are employed to compute mode shapes, which describe the spatial distribution of the wavefield, and force distributions, which represent the distribution of forces acting on the waveguide cross-section. If the left beam side has n degrees of freedom, the procedure involves solving a system of $2n$ equations. A pseudo-code is reported in Algorithm 1.

III. Numerical Analysis

A. Sandwich Beam

1. Numerical Implementation

The structure considered herein is a sandwich beam, partially analyzed by Filippi *et al.* [32]. It has rectangular cross-section dimensions equal to 0.116 m along x-axis and 0.055 m along z-axis. The sandwich material package is assumed to be made up of a soft-core 0.05 m thick, embedded between two stiff layers (skins) with a thickness of 0.0025 m each; the core is assumed to have Young's modulus $E = 0.094\,\text{GPa}$, Poisson's ratio $\nu = 0.3$, and density $\rho = 101\,\text{kg}\,\text{m}^{-3}$, while the skin layers exhibit Young's modulus $E = 9.8\,\text{GPa}$, Poisson's ratio $\nu = 0.3$, and density $\rho = 1580\,\text{kg}\,\text{m}^{-3}$. The waveguide portion considered for numerical simulations (0.002 m long) is discretized by utilizing one cubic beam element (1-B4), while the cross-section, which is schematically depicted in Fig. 1a, is modeled with Lagrange-type elements. Aiming at the identification of the optimal number of cross-section elements, a mesh converge analysis has been performed, for both modal and static cases and neglecting geometrical nonlinearity. In this context, results through five increasingly-refined meshes, respectively accounting for 12, 32, 72, 112 and 180 Lagrange-type elements, have been obtained in terms of percentage error, computed as the absolute difference of the target performance (i.e., the normalized maximum displacement in the static analysis, or the first eigenfrequency in the modal one) among

Algorithm 1 Wave dispersion algorithm using CUF.

Input:
Material properties (E, ν, ρ)
Geometrical properties (cross-section, beam length, etc.)
Prestress level
Number of elements and nodes
Wave frequencies (ω)
Step 1: Initialize parameters
Define the mesh (elements, nodes) and boundary conditions
Set the expansion functions for displacements using CUF
Initialize prestress state in the structure
Step 2: Assemble matrices
for each element **do**
    Compute the mass matrix M
    Compute the stiffness matrix K (including geometric nonlinear terms)
    Compute the damping matrix C (if necessary)
end for
Combine element matrices to form global matrices:
  Global stiffness matrix (K_{global})
  Global mass matrix (M_{global})
  Global damping matrix (C_{global}, if needed)
Step 3: Apply prestress effects
Modify the global stiffness matrix (K_{global}) to account for prestress: $K_{\text{global}} = K_{\text{global}} + K_{\text{prestress}}$
Update boundary conditions for the prestressed state
Step 4: Solve the eigenvalue problem
Solve for eigenvalues (λ_y) and eigenvectors (mode shapes, ϕ) by solving the system: $[K_{\text{global}} - \lambda_y^2 \cdot M_{\text{global}}] \cdot \phi = 0$
For each wave frequency (ω), compute the wavenumber (k) using the relation: $\lambda_y = e^{-j \cdot k \cdot \Delta}$
Step 5: Post-process results
Extract the dispersion relations: plot frequency (ω) versus wavenumber (k)
Analyze mode shapes for each frequency and wavenumber
Identify key wave propagation characteristics (e.g., mode veering, crossing, etc.)
Output:
Dispersion relations (ω vs. k)
Mode shapes for each frequency and wavenumber
Effect of prestress on wave propagation

two subsequently-refined meshes, normalized with reference to the value related to the coarser one of them. From this point of view, Figure 2 shows that the convergence in static analyses is more critical, it being achieved using 180 Lagrange-type elements, which lead to a percentage error smaller than 5%; therefore, such a discretization is chosen for all analyses that follow for this cross-section.

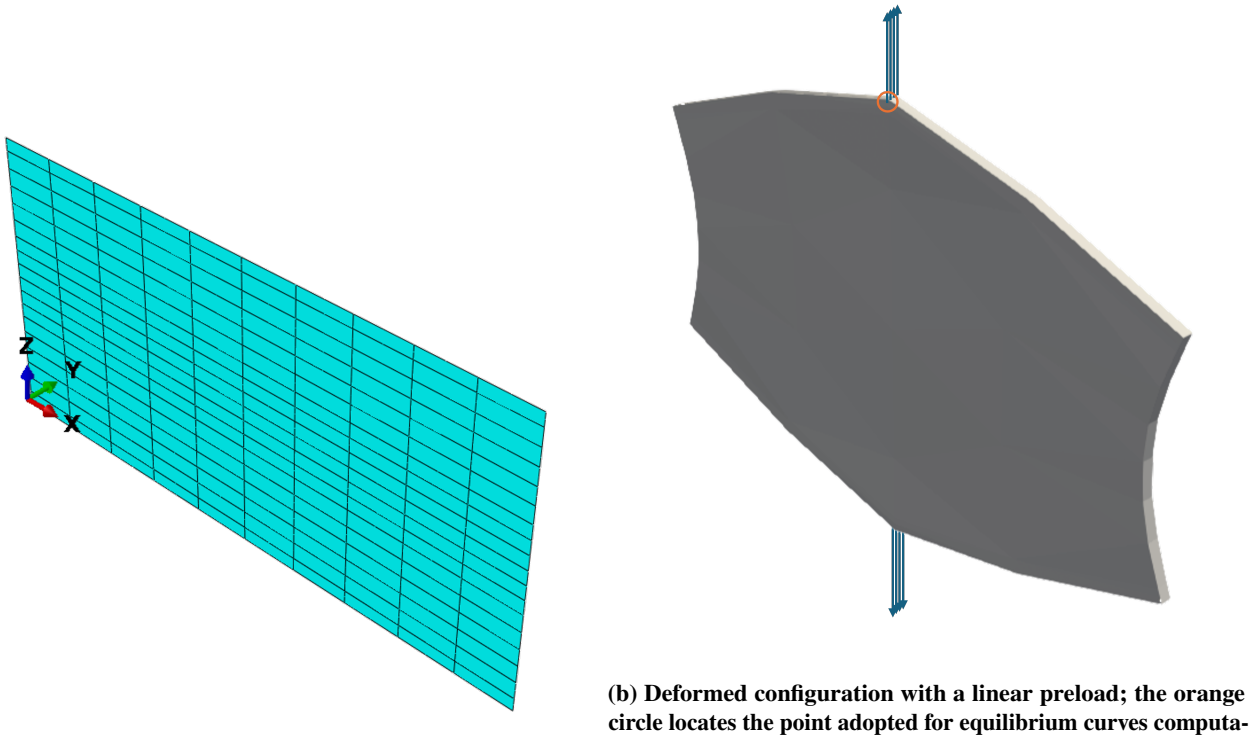

(a) 180-LE9 cross-section model.

(b) Deformed configuration with a linear preload; the orange circle locates the point adopted for equilibrium curves computation.

Fig. 1 Undeformed and linearly preloaded configurations of the sandwich beam waveguide portion.

To investigate the wave propagation characteristics of such a structure according to the different types of geometrical nonlinearity, the sandwich beam waveguide portion is then preloaded with a traction load equal to 1 N, which is symmetrical respect to the x-axis, applied on the nodes with coordinates reported in Table 1, and equally divided among the two sides of the structure; such a preload leads to a deformation that, for the linear case, is illustrated in Fig. 1b.

2. Results and Discussion

Initially, the first three cross-sectional modal shapes of the unstressed, linear, and full nonlinear sandwich beam waveguide portion with prestress equal to 500 N are investigated and shown in Fig. 3.

Aiming at achieving an external numerical validation, also dynamic response results tested in form of modal analysis by means of natural frequencies and mode shapes evaluation obtained through the commercial finite element code Abaqus are plotted; in particular, these values have been obtained by adopting 6-DoF quadratic shell elements and by neglecting geometric nonlinearity. The comparison with the correspondent CUF computed result without prestress,

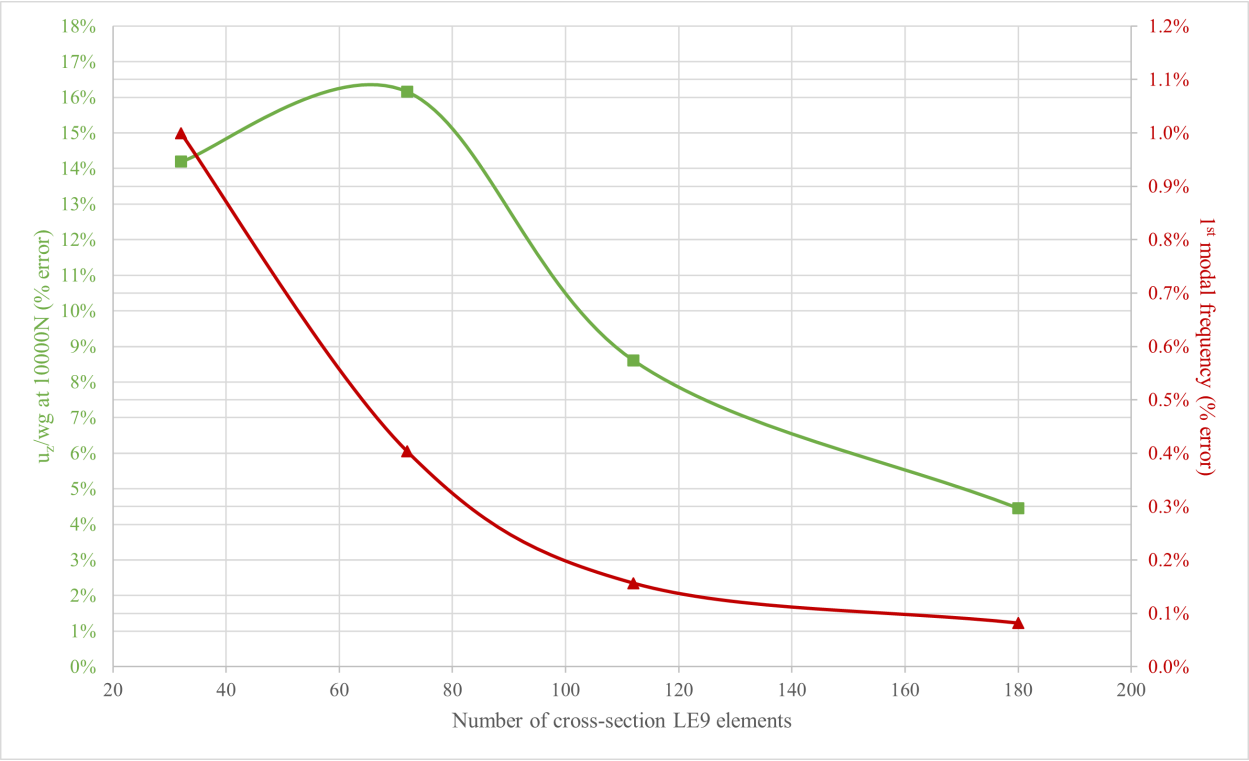

Fig. 2 LE9 mesh convergence of the sandwich beam cross-section model, neglecting geometrical nonlinearity.

Table 1 Node coordinates of the sandwich beam waveguide portion on which the preload is applied.

ID	x[m]	y[m]	z[m]	[N]
1	0.058	0	0	−0.125
2	0.058	0	0.055	0.125
3	0.058	0.000667	0	−0.125
4	0.058	0.000667	0.055	0.125
5	0.058	0.001333	0	−0.125
6	0.058	0.001333	0.055	0.125
7	0.058	0.002	0	−0.125
8	0.058	0.002	0.055	0.125

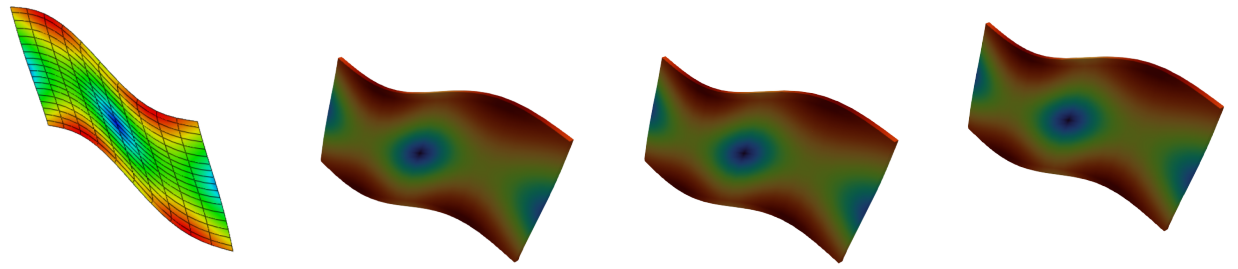

(a) First modal shape of the beam shell cross-section modeled in Abaqus, 2933 Hz**.**

(b) First modal shape of the beam without prestress, 2931 Hz**.**

(c) First modal shape of the linear beam with prestress equal to 500 N**,** 2960 Hz**.**

(d) First modal shape of the full nonlinear beam with prestress equal to 500 N**,** 2965 Hz**.**

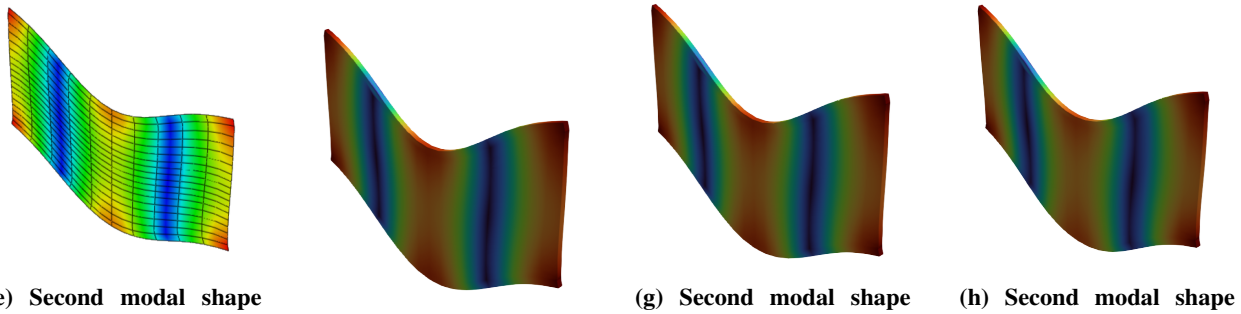

(e) Second modal shape of the beam shell cross-section modeled in Abaqus, 3208 Hz**.**

(f) Second modal shape of the beam without prestress, 3227 Hz**.**

(g) Second modal shape of the linear beam with prestress equal to 500 N**,** 3229 Hz**.**

(h) Second modal shape of the full nonlinear beam with prestress equal to 500 N**,** 3325 Hz**.**

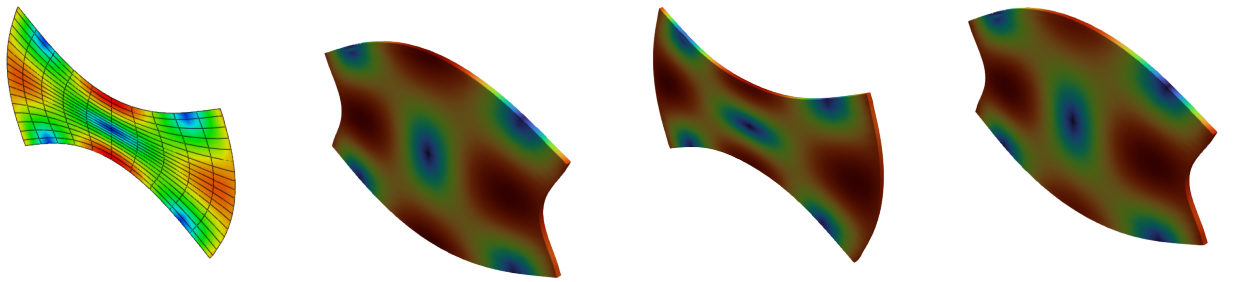

(i) Third modal shape of the beam shell cross-section modeled in Abaqus, 4123 Hz**.**

(j) Third modal shape of the beam without prestress, 4230 Hz**.**

(k) Third modal shape of the linear beam with prestress equal to 500 N**,** 4272 Hz**.**

(l) Third modal shape of the full nonlinear beam with prestress equal to 500 N**,** 4302 Hz**.**

Fig. 3 First three cross-sectional modal shapes of the unstressed (first column), linear (second column), and full nonlinear (third column) sandwich beam waveguide portion with prestress equal to 500 N**.**

represented by the second column in Figure 3 and by black markers in Figure 4, shows an almost perfect agreement, the maximum percentage shift of CUF results without prestress respect to Abaqus ones being equal to about 4%, considering both modal and static analyses.

Different acoustic-structural behaviors can be addressed by eventually nullifying (white dots in Fig. 4) or adding (black dots in Fig. 4)) the nonlinear terms of the full 3D Green–Lagrange strains matrix [35]. For clarity, the first (left) Matrix 1 is the full nonlinear one, while Matrix 5 is the linearized one. The equilibrium curves of the sandwich beam waveguide portion for various geometrical nonlinear approximations traced in Fig. 4 are obtained by computing the displacement u_z of the node with ID 2 (Table 1) along z direction, normalized respect to the waveguide portion length $wg = 0.002$ m.

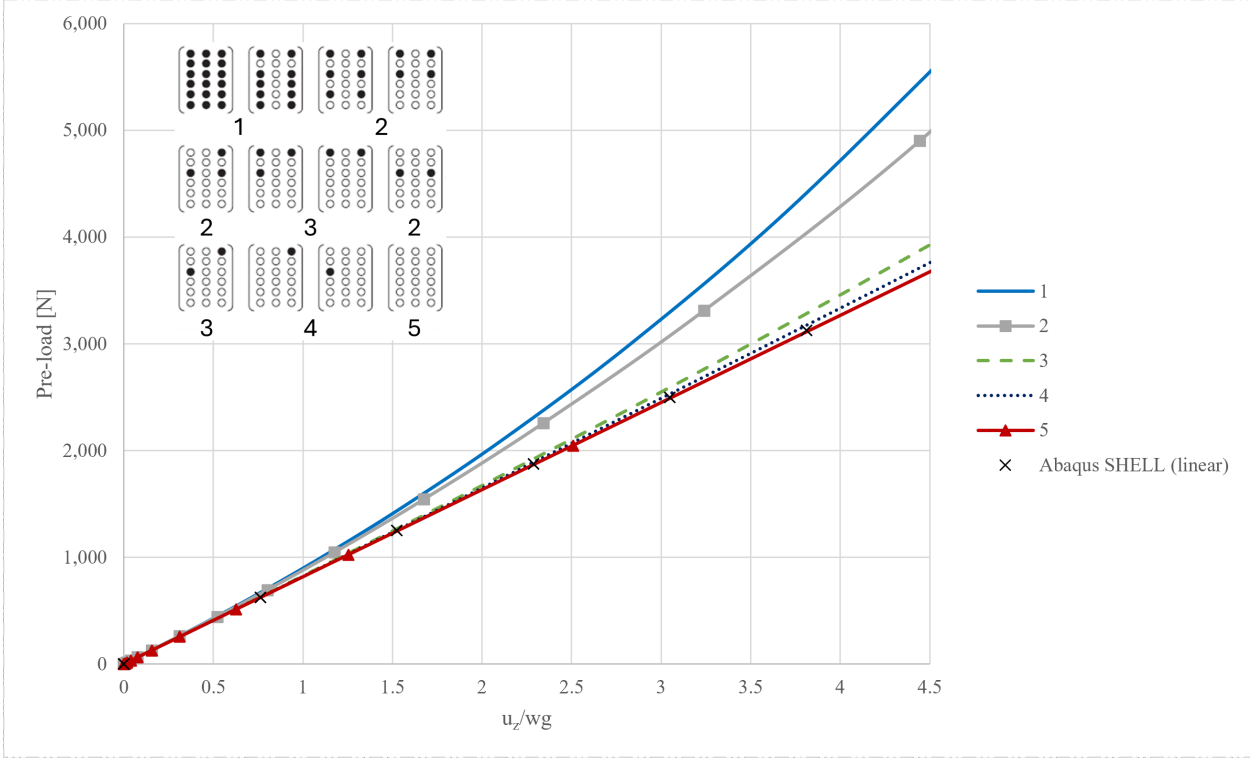

Fig. 4 Equilibrium curves of the sandwich beam waveguide portion for various geometrical nonlinear approximations.

It can be noticed that all types of nonlinearity induce a hardening behavior in the structure, which increases with the preload. This happens due to an increase in the dynamic stiffness properties of the sample. The induced structural hardening behavior directly leads to a variation in modal frequencies as highlighted in Fig. 5, where the natural frequencies of three selected modes of the sandwich beam linear waveguide portion are calculated across several preloads. These results show that different values of the applied preload on the examined sandwich beam waveguide portion lead to a mode crossing phenomenon of the first two modes at around 5500 N. Indeed, under such conditions, the structure is widely deformed; then its mechanical and acoustic behavior differs, mainly in the full nonlinear case, from that related to the same system without applied preload. A Modal Assurance Criterion (MAC) related to the linear

case is represented in Fig. 6, highlighting the modes behavior of the sandwich beam waveguide portion (constrained in the $x - z$ plane) according to different preloads (whose values are listed in Table 2).

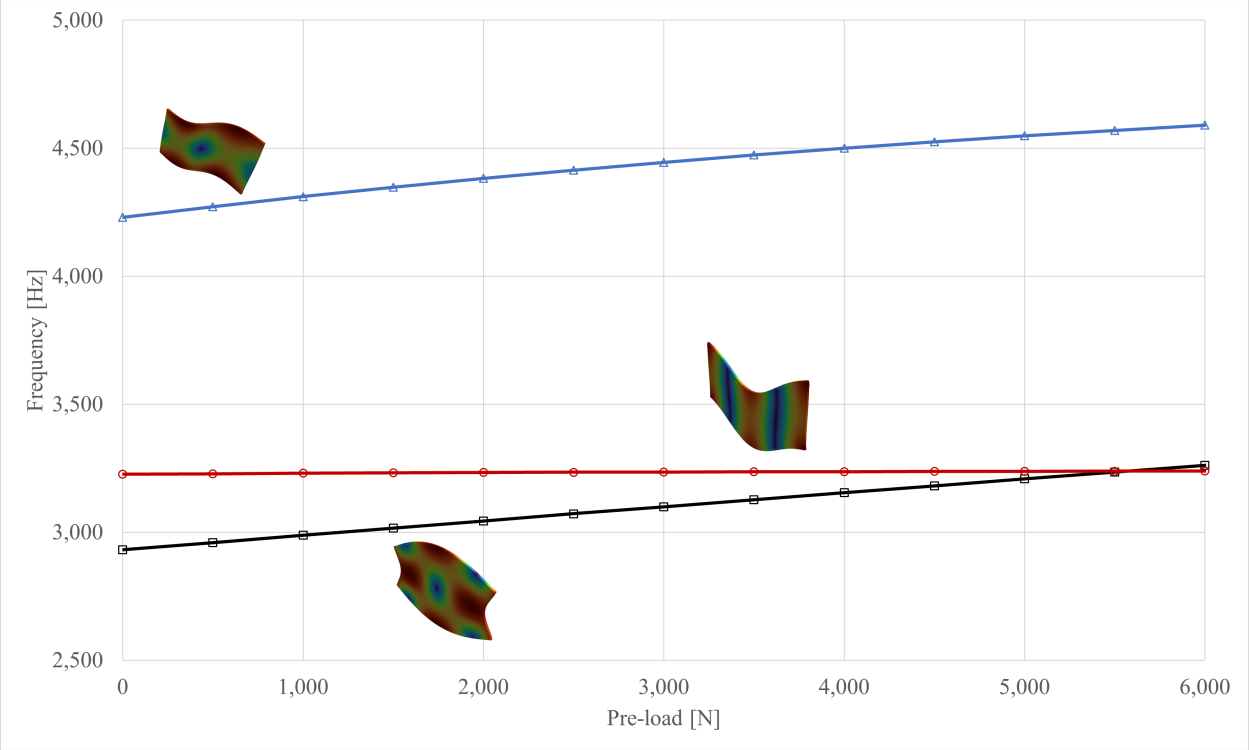

Fig. 5 Natural frequencies of the sandwich beam linear waveguide portion as functions of preload.

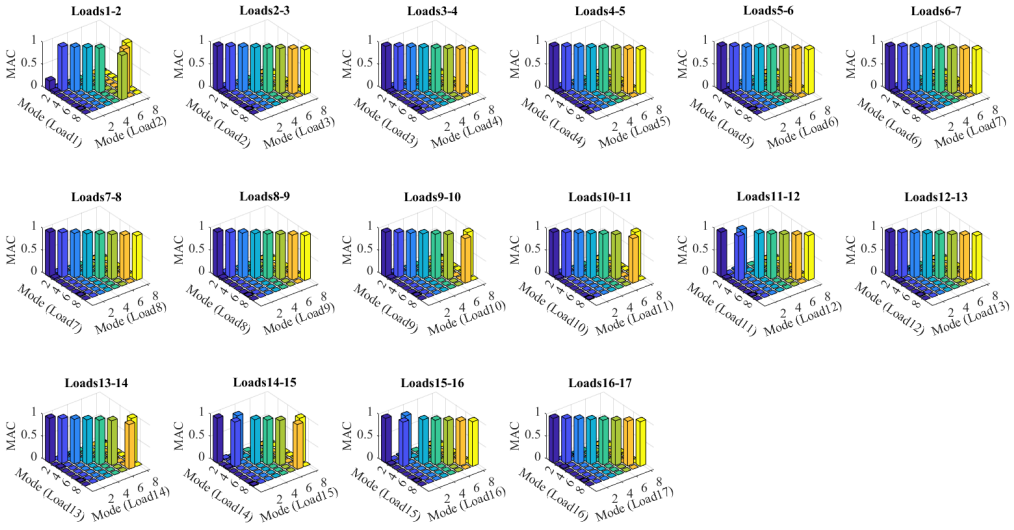

Fig. 6 MAC between modes of the sandwich beam linear waveguide portion at subsequent preloads.

Table 2 Preload values considered on the sandwich beam waveguide portion for linear and nonlinear cases.

Load	Linear case [N]	Full nonlinear case [N]
1	0	0
2	625	1
3	1250	3
4	1875	7
5	2500	15
6	3125	31
7	3750	63
8	4375	128
9	5000	260
10	5625	438
11	6250	682
12	6875	1017
13	7500	1478
14	8125	2116
15	8750	3000
16	9375	4228
17	10000	5934

Afterward, dispersion diagrams of the one-dimensional waveguide accounting for different nonlinearities are presented on the $f - k$ plane, where f is the frequency and $k = \frac{2\pi}{\lambda}$ is the wavenumber, with λ being the wavelength. A periodic behavior is assumed along the waveguide direction, thus leading to the representation of an infinite beam whose cross-section lies in the x-z plane and principal axis is directed along y, with reference to the axes system depicted in Fig. 1a. As illustrated in Fig. 7a, WFEM applied to such a CUF-modeled full nonlinear structure provides results in terms of flexural (curves (a) and (b)), torsional (curve (c)), and axial (curve (d)) wave modes; these results perfectly agree with those previously calculated by Filippi *et al.* [32]. Fig. 7b highlights that, for increasing preload magnitude, due to its structural stiffening effect, the same wave modes behave at higher frequencies.

B. Metallic Portal Beam

1. Numerical Implementation

The structure considered herein is a portal box beam. It has cross-section outer dimensions equal to 0.102 m along x-axis and 0.052 m along z-axis, and wall thickness equal to 0.002 m. The material is an aluminum with Young's modulus $E = 71$ GPa, Poisson's ratio $\nu = 0.33$, and density $\rho = 2700\,\mathrm{kg\,m^{-3}}$. The waveguide portion considered for numerical simulations (0.001 m long) is discretized by utilizing one linear beam element (1-B2), while the cross-section, which is schematically depicted in Fig. 8a, is modeled with Lagrange-type elements. With the objective to identify of the optimum number of cross-section elements, a mesh converge analysis has been performed for both modal and static

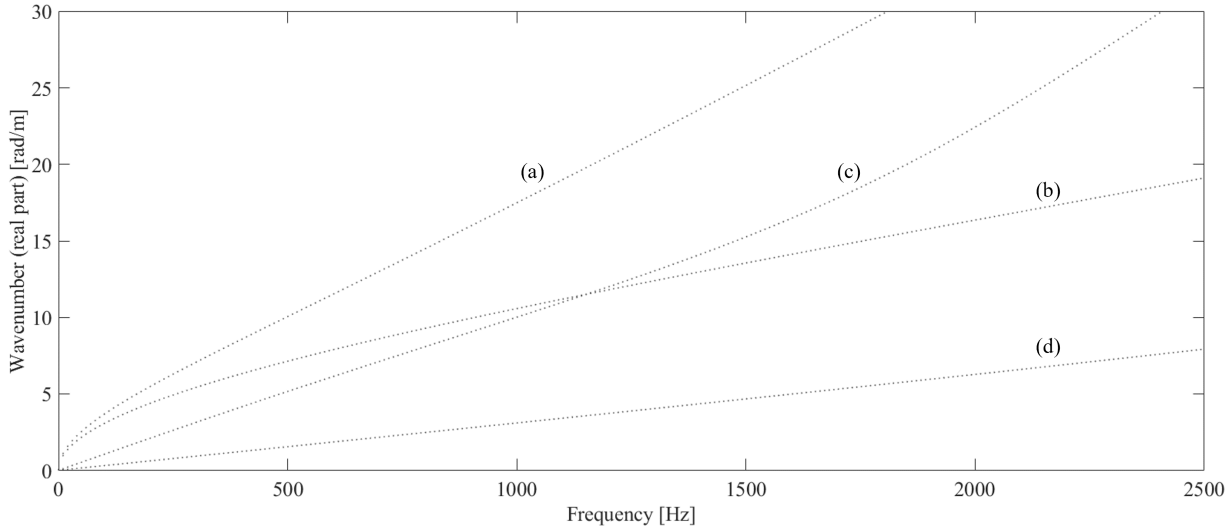

(a) Prestress = 0 N. Wave modes: (a) flexural - x; (b) flexural- z; (c) torsional; (d) axial.

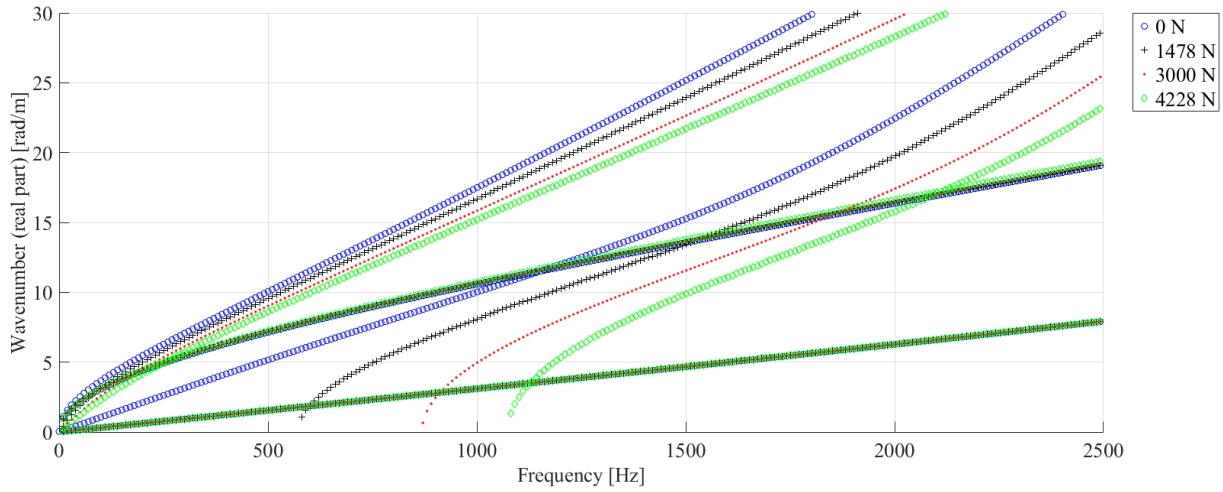

(b) Full nonlinear case subjected to four different load magnitudes.

Fig. 7 Dispersion relations of the sandwich beam as functions of the applied preload, computed by Wave Finite Element Method.

cases, while geometrical nonlinearity is neglected. In this framework, results are obtained as percentage error, whose calculation has previously been defined; two increasingly refined meshes have been considered, respectively accounting for 14 and 22 Lagrange-type elements, the second one being already sufficient to achieve a percentage error smaller than 1%. Thus, such a discretization is chosen for all the following analyses of this cross-section.

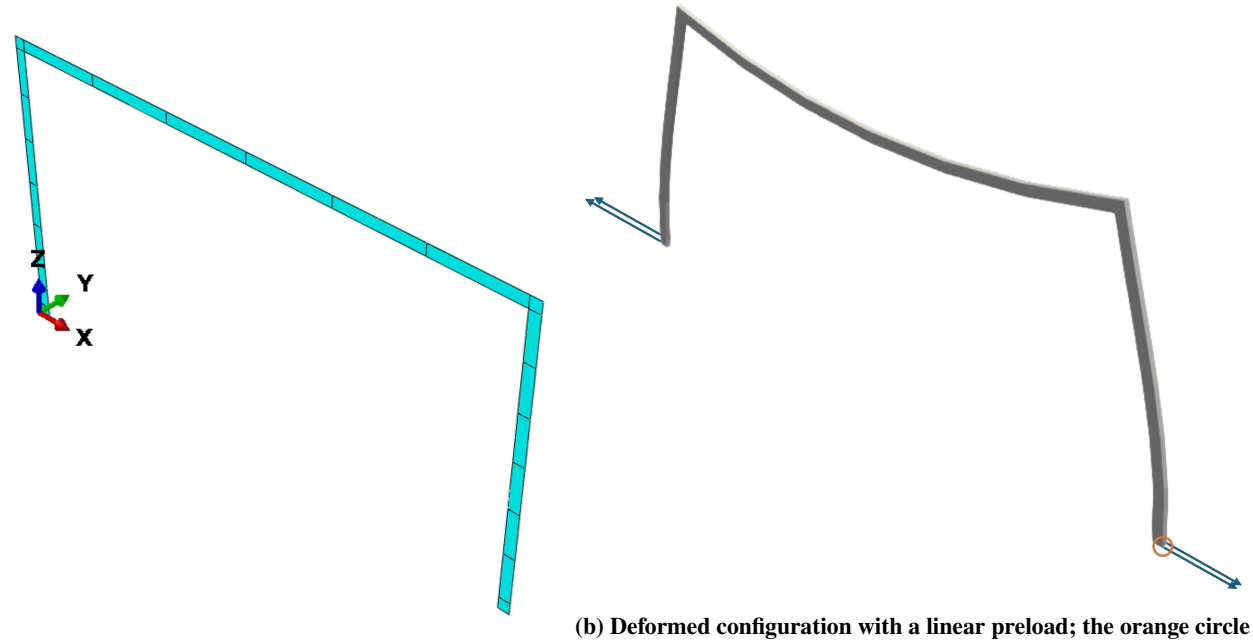

(a) 22-LE9 cross-section model.

(b) Deformed configuration with a linear preload; the orange circle locates the point adopted for equilibrium curves computation.

Fig. 8 Undeformed and linearly preloaded configurations of the metallic portal beam waveguide portion.

To investigate the wave propagation characteristics of such a structure according to the different types of geometrical nonlinearity, the metallic portal beam waveguide portion is then preloaded with a traction load equal to 1 N, which is symmetrical respect to the z-axis, applied on the nodes with coordinates reported in Table 3, and equally divided among the two sides of the structure; such a preload leads to a deformation that, for the linear case, is illustrated in Fig. 8b.

Table 3 Node coordinates of the metallic portal beam waveguide portion on which the preload is applied.

ID	x[m]	y[m]	z[m]	[N]
1	0	0	0	−0.25
2	0	0.001	0	−0.25
3	0.102	0	0	0.25
4	0.102	0.001	0	0.25

2. Results and Discussion

Initially, the first three cross-sectional modal shapes of the unstressed, linear, and full nonlinear metallic portal beam waveguide portion with prestress equal to 500 N are investigated and shown in Fig. 9.

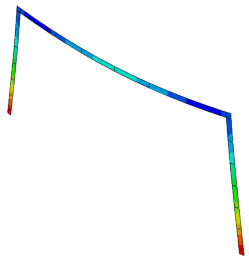

(a) First modal shape of the beam shell cross-section modeled in Abaqus, 267 Hz**.**

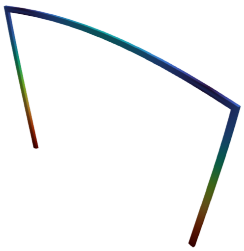

(b) First modal shape of the beam without prestress, 283 Hz**.**

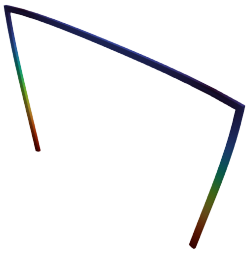

(c) First modal shape of the linear beam with prestress equal to 500 N**,** 513 Hz**.**

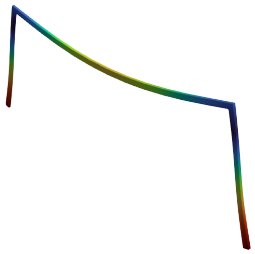

(d) First modal shape of the full nonlinear beam with prestress equal to 500 N**,** 1053 Hz**.**

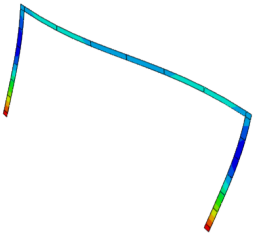

(e) Second modal shape of the beam shell cross-section modeled in Abaqus, 550 Hz**.**

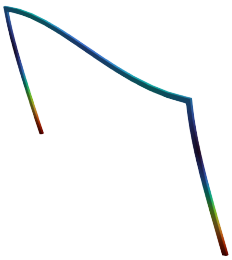

(f) Second modal shape of the beam without prestress, 583 Hz**.**

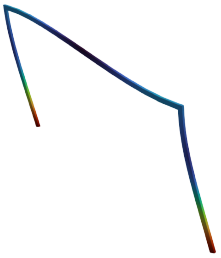

(g) Second modal shape of the linear beam with prestress equal to 500 N**,** 767 Hz**.**

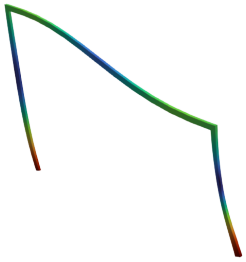

(h) Second modal shape of the full nonlinear beam with prestress equal to 500 N**,** 1566 Hz**.**

(i) Third modal shape of the beam shell cross-section modeled in Abaqus, 1091 Hz**.**

(j) Third modal shape of the beam without prestress, 1058 Hz**.**

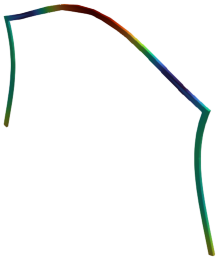

(k) Third modal shape of the linear beam with prestress equal to 500 N**,** 1774 Hz**.**

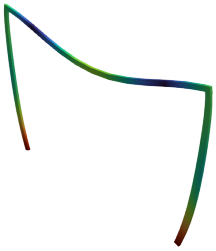

(l) Third modal shape of the full nonlinear beam with prestress equal to 500 N**,** 1812 Hz**.**

Fig. 9 First three cross-sectional modal shapes of the unstressed (first column), linear (second column), and full nonlinear (third column) metallic portal beam waveguide portion with prestress equal to 500 N**.**

Different acoustic-structural behaviors can be addressed by eventually nullifying (white dots in Fig. 10) or adding (black dots in Fig. 10)) the nonlinear terms of the full 3D Green–Lagrange strains matrix [35]. The equilibrium curves of the metallic portal beam waveguide portion for various geometrical nonlinear approximations traced in Fig. 10 are obtained by computing the displacement u_x of the node with ID 3 (Table 3) along x direction, normalized respect to the cross-section wall thickness $w = 0.002$ m. Aiming at achieving an external numerical validation, results obtained through the commercial finite element code Abaqus are also plotted; specifically, these values are obtained by adopting 6-DoF quadratic shell elements and neglecting geometric nonlinearity. The comparison with the correspondent CUF computed result without prestress, represented by the second column in Figure 9 and by black markers in Figure 10, shows an almost perfect agreement, the maximum percentage shift of CUF results without prestress respect to Abaqus ones being equal to about 6%, considering both modal and static analyses.

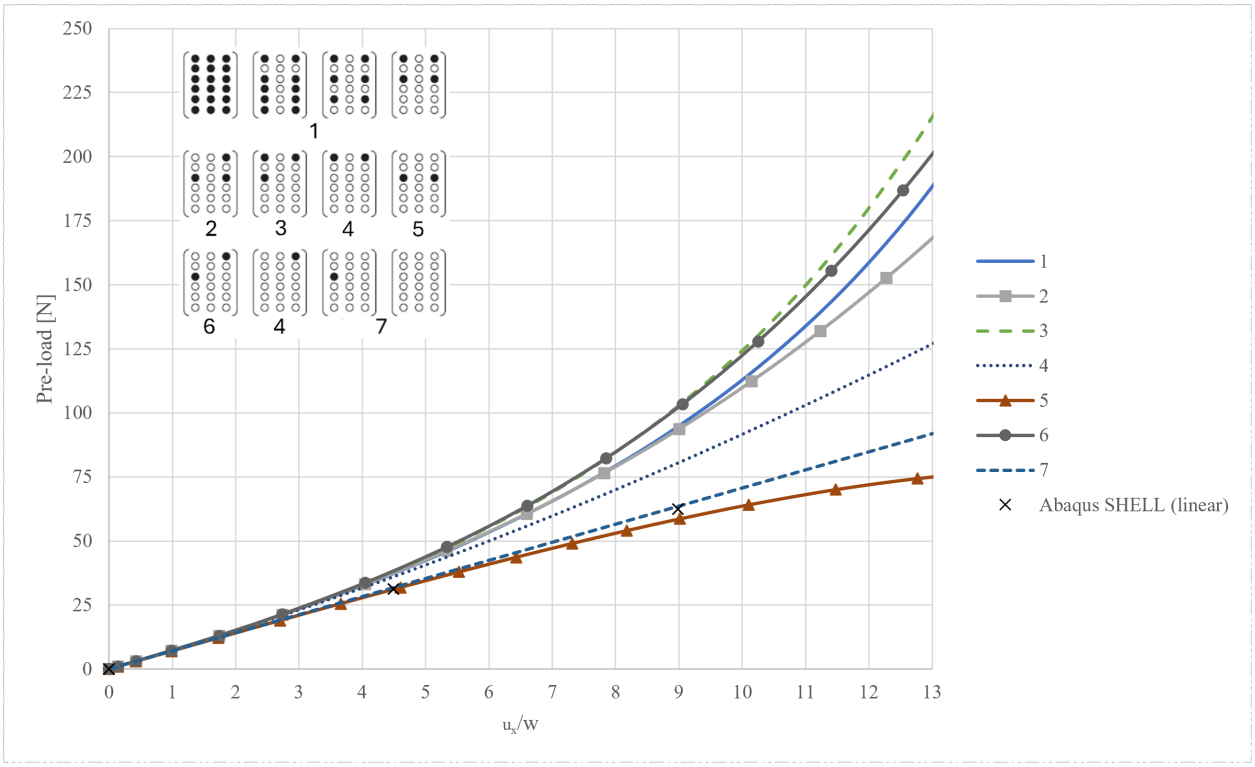

Fig. 10 Equilibrium curves of the metallic portal beam waveguide portion for various geometrical nonlinear approximations.

Again, it can be noticed that most types of nonlinearity, except for Matrix 5, induce a hardening behavior in the structure, which increases with the preload. In Fig. 11, natural frequencies of three selected modes of the metallic portal beam linear waveguide portion are calculated across several preloads. Moreover, a MAC related to the linear case is represented in Fig. 12, highlighting the modes behavior of the metallic portal beam waveguide portion (constrained in the $x - z$ plane) according to different preloads (whose values are listed in Table 4). It should be pointed out that the metallic portal beam analyzed herein is fairly similar to the single-arched metallic beam analyzed by Augello and

Carrera [36], with which it also qualitatively shares results in terms of equilibrium curves.

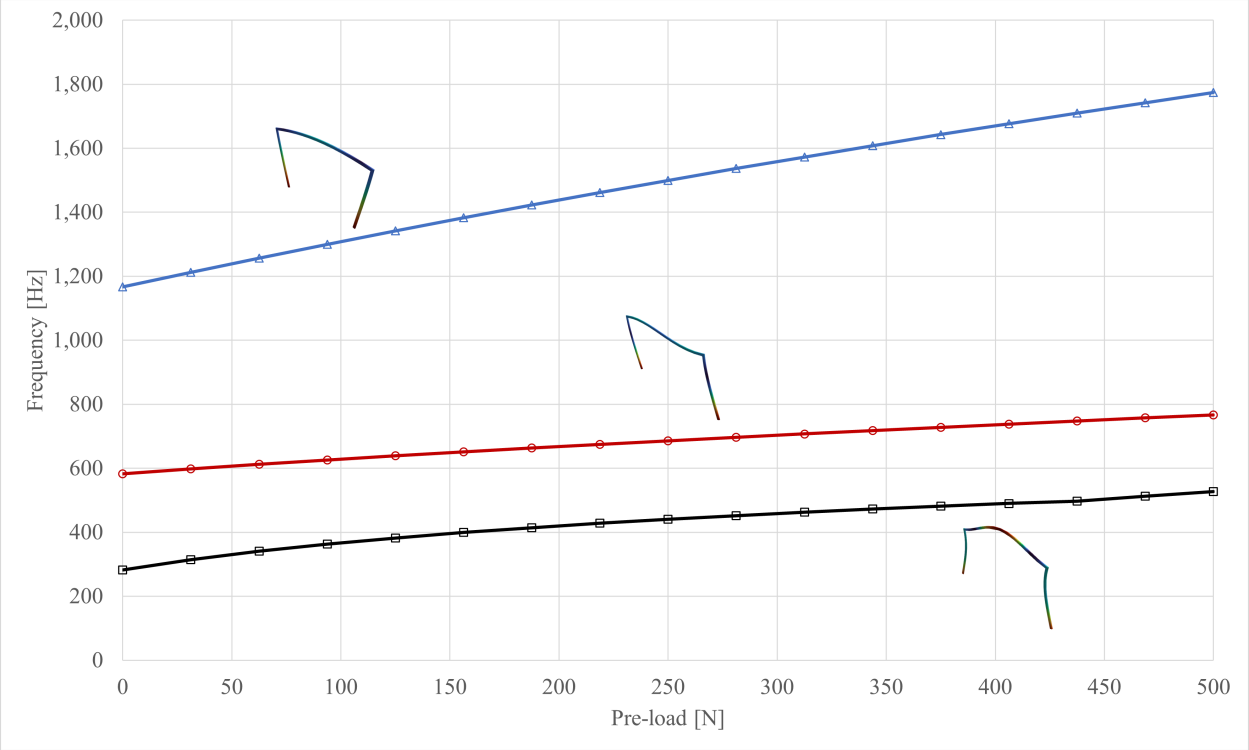

Fig. 11 Natural frequencies of the metallic portal beam linear waveguide portion as functions of preload.

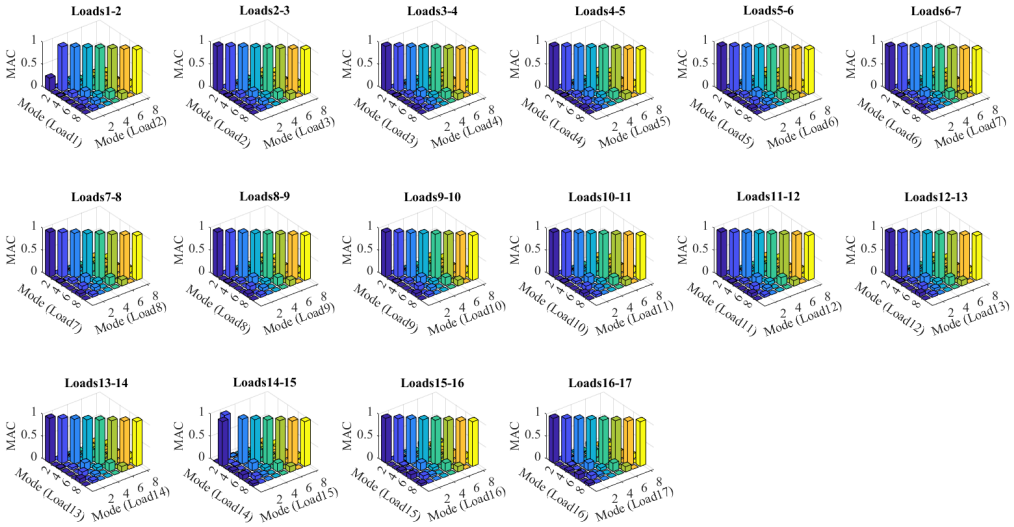

Fig. 12 MAC between modes of the metallic portal beam linear waveguide portion at subsequent preloads.

Afterward, dispersion diagrams of the one-dimensional waveguide accounting for different nonlinearities are

Table 4 Preload values considered on the metallic portal beam waveguide portion for linear and nonlinear cases.

Load	Linear case [N]	Full nonlinear case [N]
1	0	0
2	31	1
3	63	3
4	94	7
5	125	13
6	156	19
7	188	28
8	219	37
9	250	50
10	281	71
11	313	94
12	348	123
13	375	157
14	406	199
15	438	250
16	469	316
17	500	400

presented on the $f - k$ plane. Again, a periodic behavior is assumed along the waveguide direction, thus leading to the representation of an infinite beam whose cross-section lies in the x-z plane and principal axis is directed along y, with reference to the axes system depicted in Fig. 8a. As illustrated in Fig. 13a, WFEM applied to such a CUF-modeled full nonlinear structure provides results in terms of flexural (curves (a) and (b)), torsional (curve (c)), axial (curve (d)), pumping (curve (e)), shell-type/torsional (curve (f)), and shell-type/flexural (curves (g) and (h)) wave modes. Fig. 13b highlights that, for increasing preload, due to structural stiffening, the same wave modes behave at higher frequencies.

C. Metallic Box Beam

1. Numerical Implementation

The structure considered herein is a metallic box beam, partially analyzed by Filippi *et al.* [32]. Its cross-section outer dimensions, material properties and waveguide portion length are the same illustrated in Section III.B.1, while the cross-section, which is schematically depicted in Fig. 14a, is modeled with Lagrange-type elements. To find the optimal number of cross-section elements, both the modal and static mesh convergence analyses have been done ignoring geometrical nonlinearity. In this framework, results are obtained as percentage error, whose calculation has been previously defined; two increasingly refined meshes have been considered, respectively accounting for 20 and 28 Lagrange-type elements, the latter being already sufficient to reach a percentage error smaller than 4%. Hence, such a discretization is chosen for all the following analyses of this cross-section.

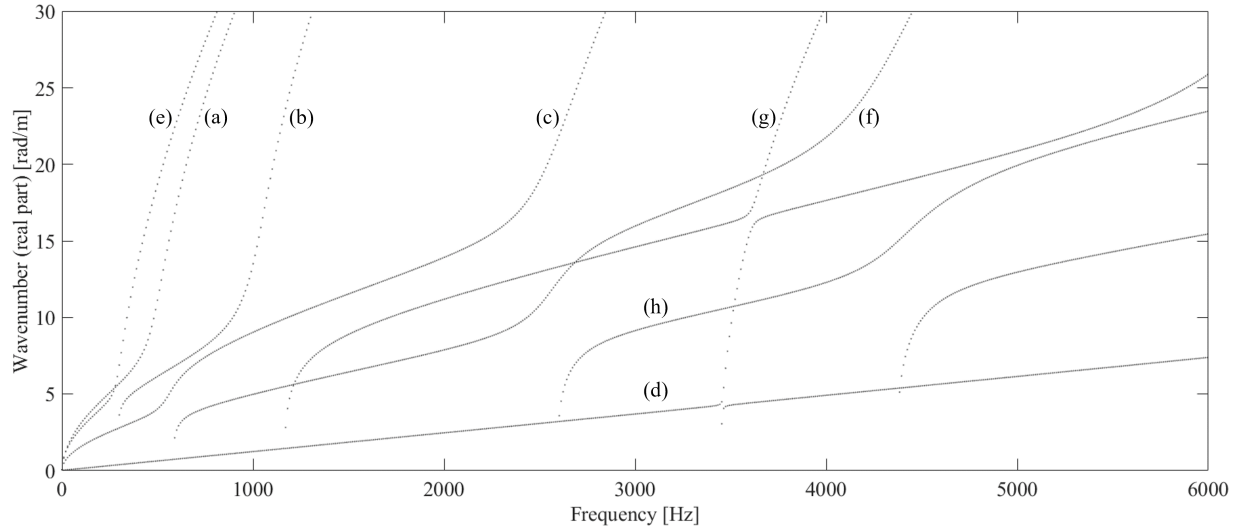

(a) Prestress = 0 N. Wave modes: (a) flexural - x; (b) flexural- z; (c) torsional; (d) axial; (e) pumping; (f) shell-type/torsional; (g) shell-type/flexural-x; (h) shell-type/flexural-z.

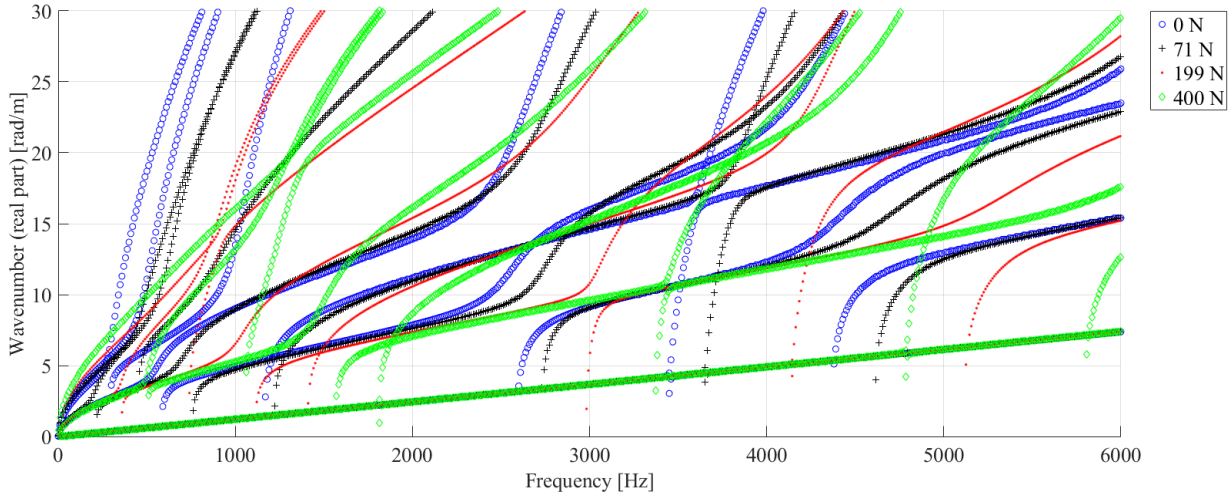

(b) Full nonlinear case subjected to four different load magnitudes.

Fig. 13 Dispersion relations of the metallic portal beam as functions of the applied preload, computed by Wave Finite Element Method.

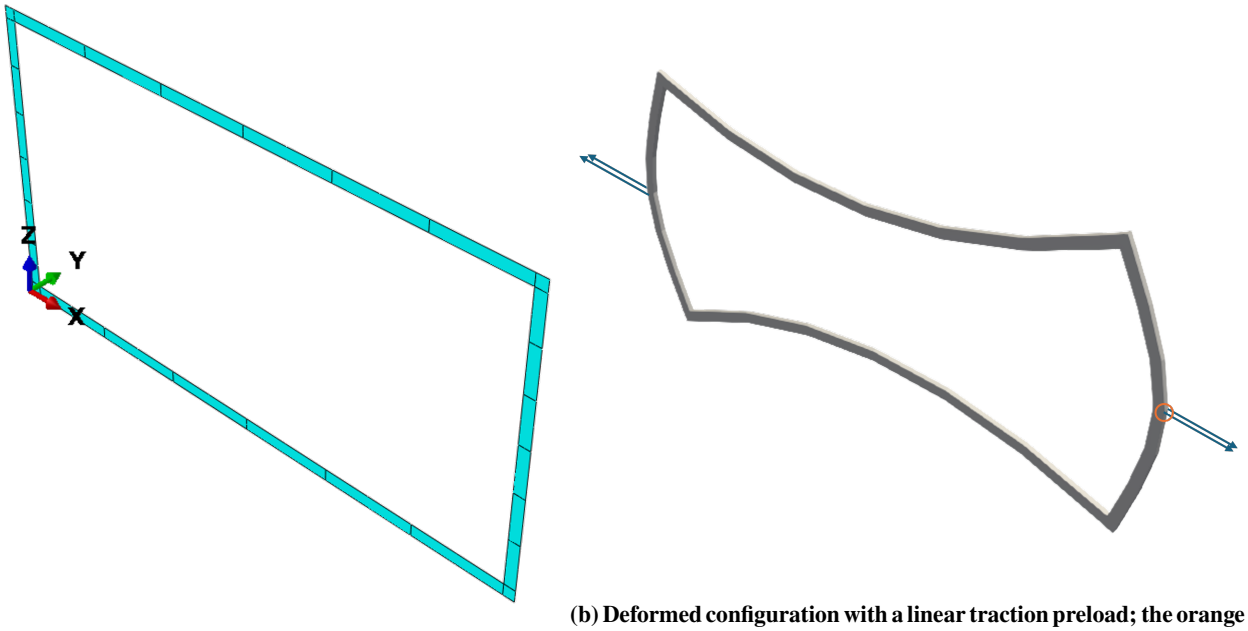

(a) 28-LE9 cross-section model.

(b) Deformed configuration with a linear traction preload; the orange circle locates the point adopted for equilibrium curves computation.

Fig. 14 Undeformed and linearly preloaded configurations of the metallic box beam waveguide portion.

To investigate the wave propagation characteristics of such a structure according to the different types of geometrical nonlinearity, the metallic box beam waveguide portion is then preloaded with a traction load equal to 1 N, which is symmetrical respect to the z-axis, applied on the nodes with coordinates reported in Table 5, and equally divided among the two sides of the structure; such a preload leads to a deformation that, for the linear case, is illustrated in Fig. 14b.

Table 5 Node coordinates of the metallic box beam waveguide portion on which the preload is applied.

ID	x[m]	y[m]	z[m]	[N]
1	0	0	0.026	−0.25
2	0	0.001	0.026	−0.25
3	0.102	0	0.026	0.25
4	0.102	0.001	0.026	0.25

2. Results and Discussion

Initially, the first three cross-sectional modal shapes of the unstressed, linear, and full nonlinear metallic box beam waveguide portion with prestress equal to 500 N are investigated and shown in Fig. 15.

Different acoustic-structural behaviors can be addressed by eventually nullifying (white dots in Fig. 16) or adding (black dots in Fig. 16)) the nonlinear terms of the full 3D Green–Lagrange strains matrix [35]. The equilibrium curves of the metallic box beam waveguide portion for various geometrical nonlinear approximations traced in Fig. 16 are obtained by computing the displacement u_x of the node with ID 3 (Table 5) along x direction, normalized respect to the

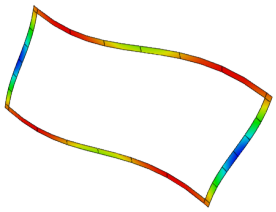

(a) First modal shape of the beam shell cross-section modeled in Abaqus, 547 Hz**.**

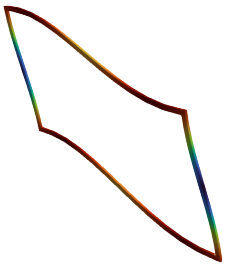

(b) First modal shape of the beam without prestress, 581 Hz**.**

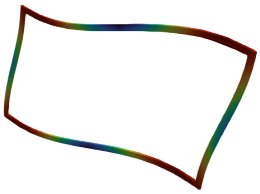

(c) First modal shape of the linear beam with prestress equal to 500 N**,** 720 Hz**.**

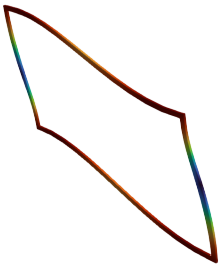

(d) First modal shape of the full nonlinear beam with prestress equal to 500 N**,** 791 Hz**.**

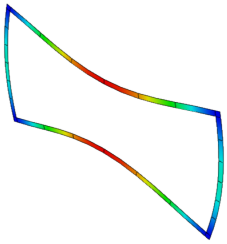

(e) Second modal shape of the beam shell cross-section modeled in Abaqus, 683 Hz**.**

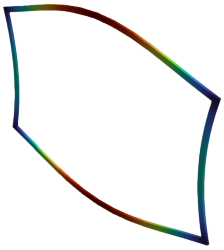

(f) Second modal shape of the beam without prestress, 729 Hz**.**

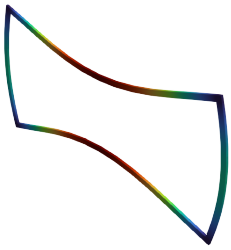

(g) Second modal shape of the linear beam with prestress equal to 500 N**,** 1041 Hz**.**

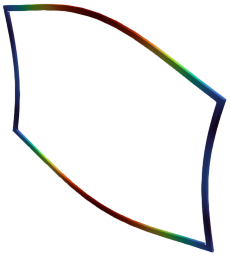

(h) Second modal shape of the full nonlinear beam with prestress equal to 500 N**,** 960 Hz**.**

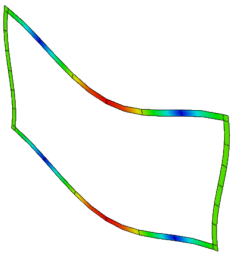

(i) Third modal shape of the beam shell cross-section modeled in Abaqus, 1231 Hz**.**

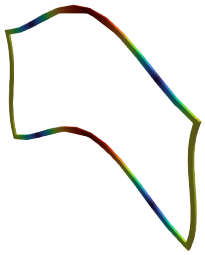

(j) Third modal shape of the beam without prestress, 1320 Hz**.**

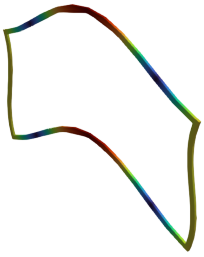

(k) Third modal shape of the linear beam with prestress equal to 500 N**,** 1730 Hz**.**

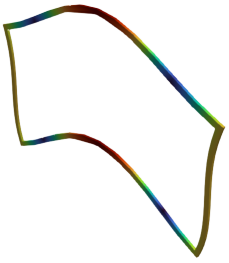

(l) Third modal shape of the full nonlinear beam with prestress equal to 500 N**,** 1567 Hz**.**

Fig. 15 First three cross-sectional modal shapes of the unstressed (first column), linear (second column), and full nonlinear (third column) metallic box beam waveguide portion with prestress equal to 500 N**.**

cross-section wall thickness $w = 0.002$ m. Also for this cross-section, results obtained by using the commercial finite element code Abaqus are plotted with the aim to perform an external numerical validation; in particular, values have been obtained by adopting 6-DoF quadratic shell elements and by neglecting geometric nonlinearity. The comparison with the correspondent CUF computed result without prestress, represented by the second column in Figure 15 and by black markers in Figure 16, shows an almost perfect agreement, the maximum percentage shift of CUF results without prestress respect to Abaqus ones being equal to about 7%, considering both modal and static analyses.

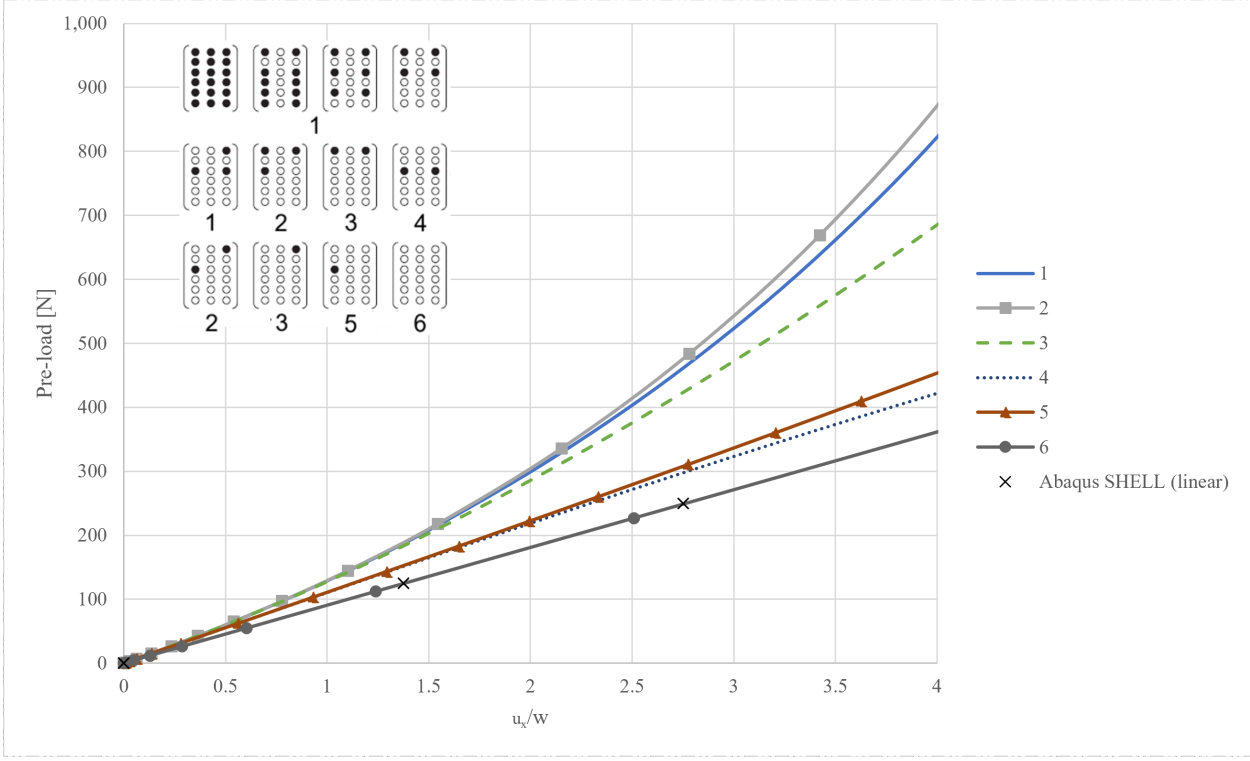

Fig. 16 Equilibrium curves of the metallic box beam waveguide portion for various geometrical nonlinear approximations.

The induced structural hardening behavior directly leads to a variation in modal frequencies as highlighted in Fig. 17, where the natural frequencies of three selected modes of the metallic box beam linear waveguide portion are calculated across several preloads, for both the linear and full nonlinear cases. Furthermore, a MAC related to the linear case is represented in Fig. 18, highlighting the modes behavior of the metallic box beam beam waveguide portion (constrained in the $x - z$ plane) according to different preloads (whose values are listed in Table 6).

Afterward, dispersion diagrams of the one-dimensional waveguide accounting for different nonlinearities are presented on the $f - k$ plane. Also in this case, a periodic behavior is assumed along the waveguide direction, thus leading to the representation of an infinite beam whose cross-section lies in the x-z plane and principal axis is directed along y, with reference to the axes system depicted in Fig. 14a. As illustrated in Fig. 19a, WFEM applied to such a CUF-modeled full nonlinear structure provides results in terms of flexural (curves (a) and (b)), torsional (curve (c)),

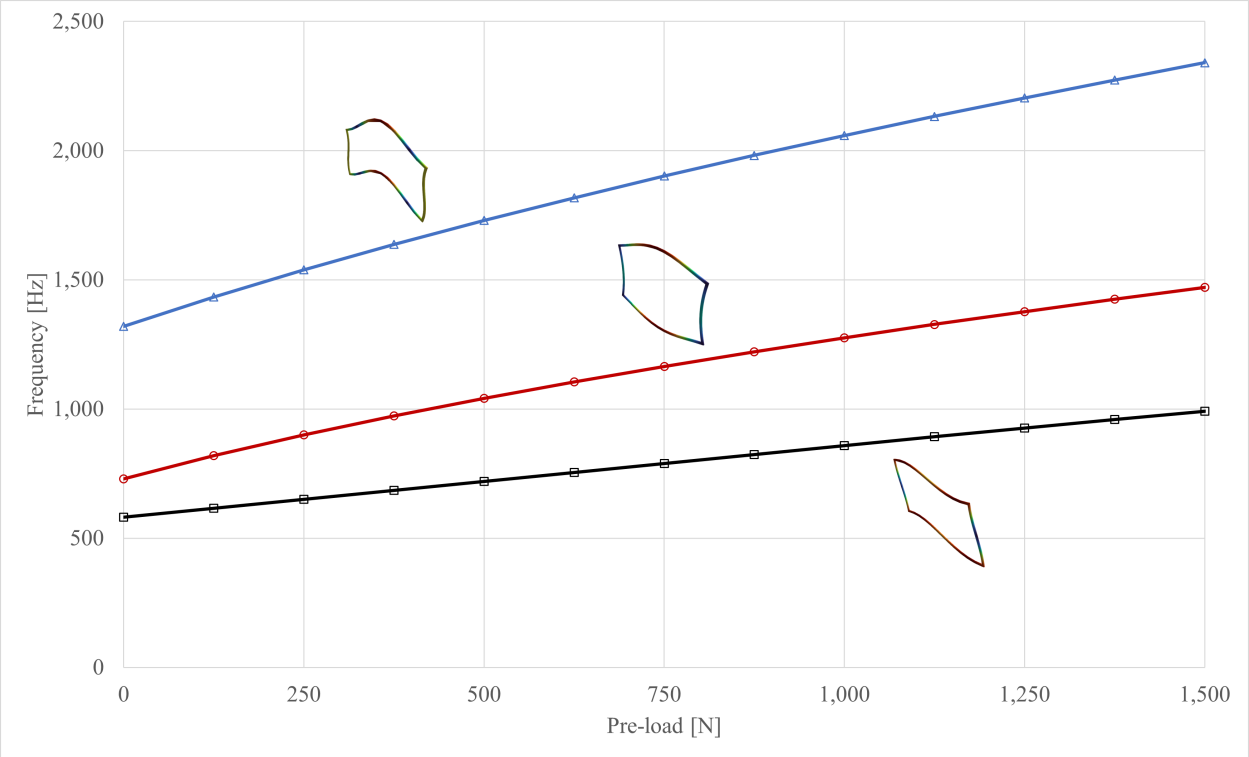

Fig. 17 Natural frequencies of the metallic box beam linear waveguide portion as functions of preload.

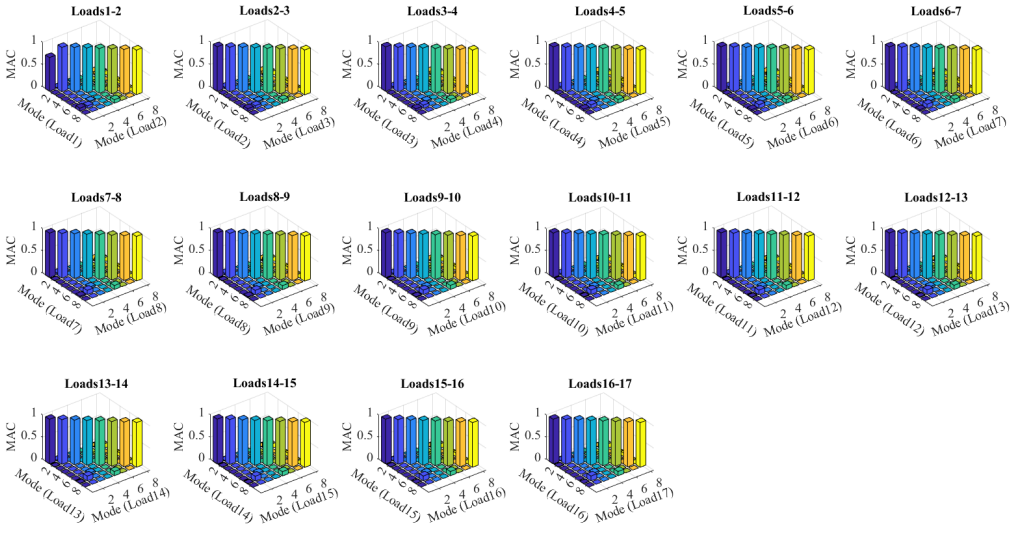

Fig. 18 MAC between modes of the metallic box beam linear waveguide portion at subsequent preloads.

Table 6 Preload values considered on the metallic box beam waveguide portion for linear and nonlinear cases.

Load	Linear case [N]	Full nonlinear case [N]
1	0	0
2	125	1
3	250	3
4	375	7
5	500	15
6	625	27
7	750	43
8	875	65
9	1000	97
10	1125	144
11	1250	215
12	1375	328
13	1500	465
14	1625	630
15	1750	829
16	1875	1070
17	2000	1358

axial (curve (d)), pumping (curve (e)), shell-type/torsional (curve (f)), and shell-type/flexural (curves (g) and (h)) wave modes; these results perfectly agree with those previously calculated by Filippi *et al.* [32]. Fig. 19b highlights that, for increasing preload magnitude, due to its structural stiffening effect, the same wave modes behave at higher frequencies; this directly leads to differences in the dispersion diagram, potentially also arising complex modal phenomena such as those already discussed when referring to Fig. 17. Notably, an applied preload may be interpreted as a numerical simplification of a combination of external effects acting upon a structure, which therefore should be accounted for when estimating its acoustic-structural response, especially if the structure is designed to reach specific tonal performance.

IV. Conclusions

A. Summary of Key Findings

This study investigates the wave propagation characteristics in prestressed structures with different geometric nonlinearities, focusing on a sandwich beam, a metallic portal beam and a metallic box beam modeled using CUF approach. Initially, the principal cross-sectional unstressed, linear, and full nonlinear modal shapes with prestress equal to 500 N are examined, revealing torsional and flexural modes. Subsequently, the equilibrium curves of the structure are traced for various geometric nonlinear approximations, demonstrating that most forms of nonlinearity induce a stiffening effect in the system, which intensifies with the preload, leading directly to a variation in modal frequencies. To further expand the scope of the present research, the dispersion relations of the examined full nonlinear structures

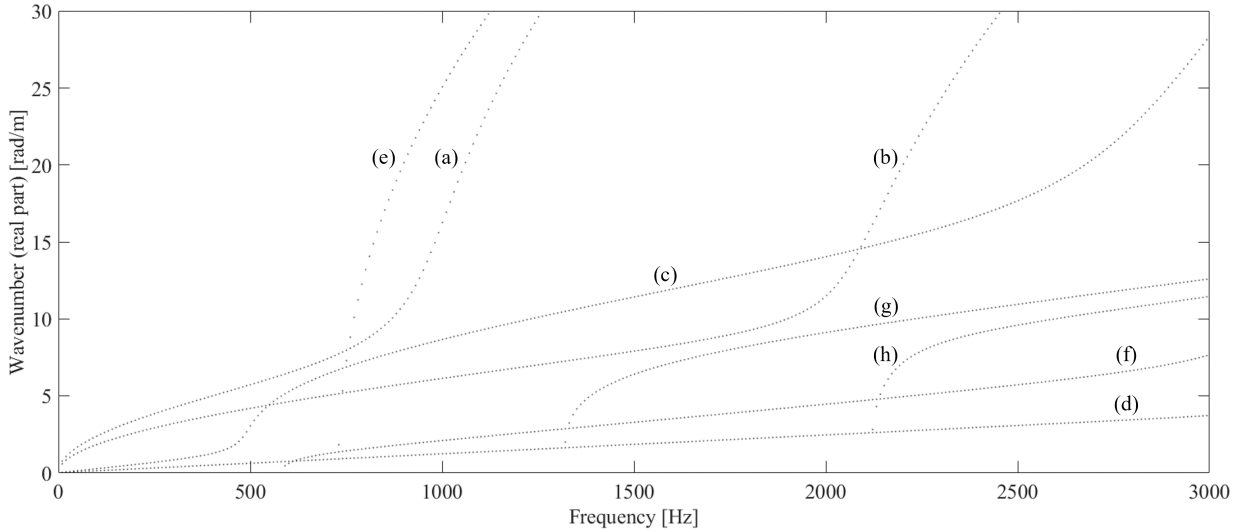

(a) Prestress = 0 N. Wave modes: (a) flexural - x; (b) flexural- z; (c) torsional; (d) axial; (e) pumping; (f) shell-type/torsional; (g) shell-type/flexural-x; (h) shell-type/flexural-z.

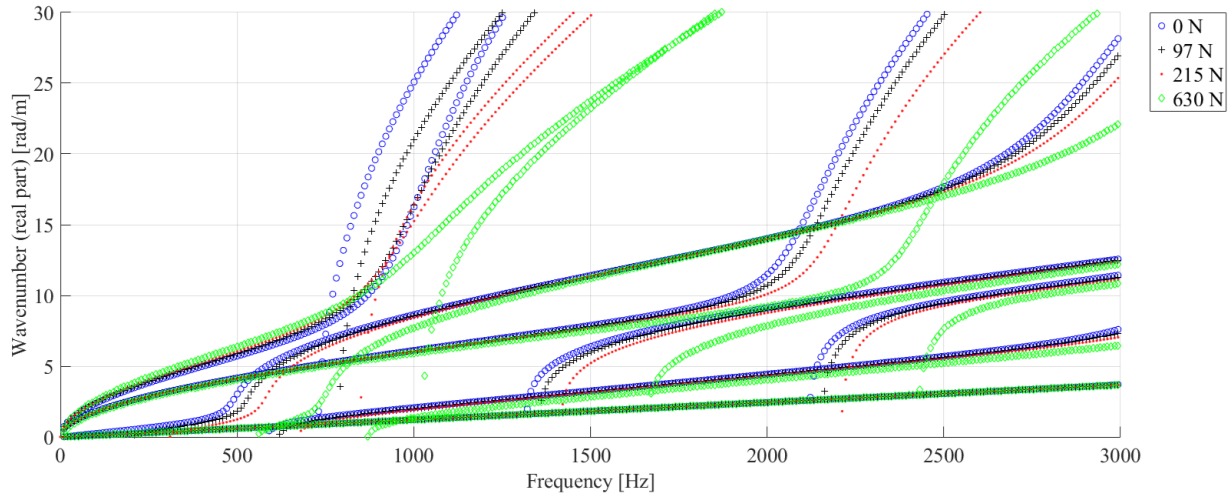

(b) Full nonlinear case subjected to four different load magnitudes.

Fig. 19 Dispersion relations of the metallic box beam as functions of the applied preload, computed by Wave Finite Element Method.

are analyzed as a function of the applied preload using WFEM, whose dynamic linear behaviors, in the case of the beams with sandwich and metallic box cross-sections, perfectly agree with those previously calculated by Filippi *et al.* [32]. This technique enables a comprehensive evaluation of wave propagation characteristics under mechanical loading conditions. The dispersion relation, a graphical representation of the relationship between wavenumber and frequency, provides valuable insights into the intricate mechanisms governing wave propagation within the waveguide. By scrutinizing dispersion curves at distinct preload levels, a deeper understanding is gained regarding the impact of mechanical loading on wave propagation through the waveguide.

In summary, the results of this study lead to a better understanding of the intricate interplay between prestress, geometric nonlinearities, and wave propagation behavior of prestressed structures, a process that contributes much toward understanding wave propagation in complex structural systems and aids in the design of prestressed structures with acoustically desired features. This acquired knowledge is of meaningful value in the waveguide design process by application, specifically those requiring either effective wave transmission or confinement. Even further, such understanding might have huge implications on the design and analysis of prestressed systems under static loads.

B. Future Perspectives

Despite the advanced developments in this research, further study still remains a lot in scope. This paper discussed only the prestressed structures, considering the simple geometric configurations, such as beams and plates. A further study will extend the analysis to more complex geometries, for instance, shells or curved beams, to understand the behavior of wave propagation in these structures. This study is mostly focused on static prestress, whereby the applied prestress remains constant. In the future, dynamic prestress can be worked on whereby prestress changes with time or some other different external loading conditions. This would provide valuable insight into wave propagation behavior in structures subjected to dynamic loads, as in the case of earthquakes and blast forces.

The core of the research lies in the effects of geometric nonlinearities on wave propagation in a prestressed structure. The next steps would involve including material nonlinearities, like plasticity and damage, in the analysis and see how they change the wave propagation behavior and hence the structural response. Such may further lead to a fuller understanding of wave propagation in prestressed structure and eventually impact the very design and analysis of prestressed systems to provide improved acoustic performance for a wide range of applications related to sound quality, noise pollution reduction, and better structural integrity.

Acknowledgments

The authors acknowledge the support of the Italian Ministry of University and Research (MUR) and the Sustainable Mobility Center (MOST) through the project PNRR - M4C2 - CNMS - Spoke 1, funded under the scheme CN00000023 - PNRR – M4C2 Inv. 1.4 with grant agreement no. 55_PRR22_1155_22_GG002138.

The authors also acknowledge the support of the Italian Ministry of University and Research (MUR) through the project TWINCRAFT - Digital Twin for Human-Centred Design of Future Aircraft, funded under the scheme PRIN 2022 with grant agreement no. 2022LXKA3R.

References

[1] Filippi, M., Magliacano, D., Petrolo, M., and Carrera, E., "Wave Propagation in Pre-Stressed Structures With Geometric Non-Linearities Through Carrera Unified Formulation," 2024. https://doi.org/10.2514/6.2024-3028.

[2] Mackerle, J., "Finite element linear and nonlinear, static and dynamic analysis of structural elements: a bibliography (1992-1995)," *Engineering computations*, Vol. 14, No. 4, 1997, p. 347 – 440. https://doi.org/10.1108/02644409710178494.

[3] Carrera, E., and Parisch, H., "An evaluation of geometrical nonlinear effects of thin and moderately thick multilayered composite shells," *Composite Structures*, Vol. 40, No. 1, 1997, p. 11 – 24. https://doi.org/10.1016/S0263-8223(97)00145-1.

[4] Carrera, E., and Zappino, E., "Carrera unified formulation for free-vibration analysis of aircraft structures," *AIAA Journal*, Vol. 54, No. 1, 2016, p. 280 – 292. https://doi.org/10.2514/1.J054265.

[5] Hui, Y., Xu, R., Giunta, G., De Pietro, G., Hu, H., Belouettar, S., and Carrera, E., "Multiscale CUF-FE2 nonlinear analysis of composite beam structures," *Computers and Structures*, Vol. 221, September 2019, p. 28 – 43. https://doi.org/10.1016/j.compstruc.2019.05.013.

[6] Pagani, A., and Carrera, E., "Unified formulation of geometrically nonlinear refined beam theories," *Mechanics of Advanced Materials and Structures*, Vol. 25, No. 1, 2018, p. 15 – 31. https://doi.org/10.1080/15376494.2016.1232458.

[7] Wu, B., Pagani, A., Chen, W., and Carrera, E., "Geometrically nonlinear refined shell theories by Carrera Unified Formulation," *Mechanics of Advanced Materials and Structures*, Vol. 28, No. 16, 2021, p. 1721 – 1741. https://doi.org/10.1080/15376494.2019.1702237.

[8] Petrolo, M., Kaleel, I., De Pietro, G., and Carrera, E., "Wave propagation in compact, thin-walled, layered, and heterogeneous structures using variable kinematics finite elements," *International Journal for Computational Methods in Engineering Science and Mechanics*, Vol. 19, No. 3, 2018, p. 207 – 220. https://doi.org/10.1080/15502287.2018.1447048.

[9] Cinefra, M., de Miguel, A. G., Filippi, M., Houriet, C., Pagani, A., and Carrera, E., "Homogenization and free-vibration analysis of elastic metamaterial plates by Carrera Unified Formulation finite elements," *Mechanics of Advanced Materials and Structures*, Vol. 28, No. 5, 2021, p. 476 – 485. https://doi.org/10.1080/15376494.2019.1578005.

[10] De Miguel, A., Cinefra, M., Filippi, M., Pagani, A., and Carrera, E., "Validation of FEM models based on Carrera Unified Formulation for the parametric characterization of composite metamaterials," *Journal of Sound and Vibration*, Vol. 498, 28 April 2021. https://doi.org/10.1016/j.jsv.2021.115979.

[11] Magliacano, D., Viscardi, M., Dimino, I., and Concilio, A., "Active vibration control by piezoceramic actuators of a car floor panel," 23rd International Congress on Sound and Vibration (ICSV23), Athens (Greece), 10-14 July 2016, p. 3382 – 3389. Paper number 982.

[12] Magliacano, D., Ouisse, M., Khelif, A., De Rosa, S., Franco, F., and Atalla, N., "Computation of wave dispersion characteristics in periodic porous materials modeled as equivalent fluids," Leuven (Belgium), 17-19 September 2018, p. 4741 – 4751.

[13] Magliacano, D., Ouisse, M., Rosa, S., Franco, F., and Khelif, A., "Investigations about the modelling of acoustic properties of periodic porous materials with the shift cell approach," Paris (France), 08-11 July 2019, p. 1112 – 1123.

[14] Catapane, G., Magliacano, D., Petrone, G., Casaburo, A., Franco, F., and De Rosa, S., "Transmission Loss Analyses on Different Angular Distributions of Periodic Inclusions in a Porous Layer," *Aerotecnica Missili & Spazio*, Vol. 100, No. 4, 2021, p. 363 – 373. https://doi.org/10.1007/s42496-021-00101-6.

[15] Magliacano, D., Catapane, G., Petrone, G., Verdière, K., and Robin, O., "Sound transmission properties of a porous metamaterial with periodically embedded Helmholtz resonators," *Mechanics of Advanced Materials and Structures*, 19 July 2023. https://doi.org/10.1080/15376494.2023.2237699.

[16] Casaburo, A., Magliacano, D., Petrone, G., Franco, F., and de Rosa, S., "Optimizing the acoustic properties of a metamaterial using machine learning techniques," Washington (United States of America), 01-05 August 2021, p. 1948 – 1959. https://doi.org/10.3397/IN2021-2294, paper number 2294.

[17] Catapane, G., Magliacano, D., Petrone, G., Casaburo, A., Franco, F., and De Rosa, S., "Semi-analytical estimation of Helmholtz resonators' tuning frequency for scalable neck-cavity geometric couplings," *CEAS Aeronautical Journal*, Vol. 13, No. 3, 2022, p. 797 – 808. https://doi.org/10.1007/s13272-022-00592-4.

[18] Catapane, G., Magliacano, D., Petrone, G., Casaburo, A., Franco, F., and De Rosa, S., "Labyrinth Resonator Design for Low-Frequency Acoustic Meta-Structures," *Mechanisms and Machine Science*, Vol. 125 MMS, 07 October 2022, p. 681 – 694. https://doi.org/10.1007/978-3-031-15758-5_70.

[19] Gei, M., Movchan, A., and Bigoni, D., "Band-gap shift and defect-induced annihilation in prestressed elastic structures," *Journal of Applied Physics*, Vol. 105, No. 6, 2009. https://doi.org/10.1063/1.3093694.

[20] Gei, M., "Wave propagation in quasiperiodic structures: Stop/pass band distribution and prestress effects," *International Journal of Solids and Structures*, Vol. 47, No. 22-23, 2010, p. 3067 – 3075. https://doi.org/10.1016/j.ijsolstr.2010.07.008.

[21] Parnell, W. J., "Pre-stressed viscoelastic composites: Effective incremental moduli and band-gap tuning," Rhodes (Greece), 19-25 September 2010, p. 837 – 840. https://doi.org/10.1063/1.3498616.

[22] Barnwell, E. G., Parnell, W. J., and David Abrahams, I., "Antiplane elastic wave propagation in pre-stressed periodic structures; tuning, band-gap switching and invariance," *Wave Motion*, Vol. 63, June 2016, p. 98 – 110. https://doi.org/10.1016/j.wavemoti.2016.02.001.

[23] Barnwell, E. G., Parnell, W. J., and Abrahams, I. D., "Tunable elastodynamic band gaps," *Extreme Mechanics Letters*, Vol. 12, April 2017, p. 23 – 29. https://doi.org/10.1016/j.eml.2016.10.009.

[24] Zhang, K., Su, Y.-c., Hou, X.-h., Meng, J.-m., and Deng, Z.-c., "Effect of pre-load on wave propagation characteristics of hexagonal lattices," *Composite Structures*, Vol. 203, 1 November 2018, p. 361 – 372. https://doi.org/10.1016/j.compstruct.2018.07.033.

[25] De Pascalis, R., Donateo, T., Ficarella, A., and Parnell, W. J., "Optimal design of phononic media through genetic algorithm-informed pre-stress for the control of antiplane wave propagation," *Extreme Mechanics Letters*, Vol. 40, October 2020. https://doi.org/10.1016/j.eml.2020.100896.

[26] Petrolo, M., and Carrera, E., "Best Spatial Distributions of Shell Kinematics Over 2D Meshes for Free Vibration Analyses," *Aerotecnica Missili & Spazio*, Vol. 99, No. 3, 2020, p. 217 – 232. https://doi.org/10.1007/s42496-020-00045-3.

[27] Nagaraj, M. H., Kaleel, I., Carrera, E., and Petrolo, M., "Elastoplastic Micromechanical Analysis of Fiber-Reinforced Composites with Defects," *Aerotecnica Missili & Spazio*, Vol. 101, No. 1, 2022, p. 53 – 59. https://doi.org/10.1007/s42496-021-00103-4.

[28] H. Cabral, P., Carrera, E., dos Santos, H. E. A. A., Galeb, P. H. G., Pagani, A., Peeters, D., and Prado, A. P., "Experimental and numerical vibration correlation of pre-stressed laminated reinforced panel," *Mechanics of Advanced Materials and Structures*, Vol. 29, No. 15, 2022, p. 2165 – 2175. https://doi.org/10.1080/15376494.2020.1853285.

[29] Wu, B., Pagani, A., Filippi, M., Chen, W., and Carrera, E., "Large-deflection and post-buckling analyses of isotropic rectangular plates by Carrera Unified Formulation," *International Journal of Non-Linear Mechanics*, Vol. 116, November 2019, p. 18 – 31. https://doi.org/10.1016/j.ijnonlinmec.2019.05.004.

[30] Pagani, A., and Carrera, E., "Large-deflection and post-buckling analyses of laminated composite beams by Carrera Unified Formulation," *Composite Structures*, Vol. 170, 15 June 2017, p. 40 – 52. https://doi.org/10.1016/j.compstruct.2017.03.008.

[31] Filippi, M., Magliacano, D., Petrolo, M., and Carrera, E., "Variable-Kinematics Finite Elements for Propagation Analyses of Two-Dimensional Waveguides," 2024. https://doi.org/10.2514/6.2024-3078.

[32] Filippi, M., Pagani, A., and Carrera, E., "High-order finite beam elements for propagation analyses of arbitrary-shaped one-dimensional waveguides," *Mechanics of Advanced Materials and Structures*, Vol. 29, No. 13, 2022, p. 1883 – 1891. https://doi.org/10.1080/15376494.2020.1842951.

[33] Carrera, E., Maiarú, M., and Petrolo, M., "Component-wise analysis of laminated anisotropic composites," *International Journal of Solids and Structures*, Vol. 49, No. 13, 2012, p. 1839 – 1851. https://doi.org/10.1016/j.ijsolstr.2012.03.025.

[34] Carrera, E., Azzara, R., Daneshkhah, E., Pagani, A., and Wu, B., "Buckling and post-buckling of anisotropic flat panels subjected to axial and shear in-plane loadings accounting for classical and refined structural and nonlinear theories," *International Journal of Non-Linear Mechanics*, Vol. 133, July 2021. https://doi.org/10.1016/j.ijnonlinmec.2021.103716.

[35] Carrera, E., Pagani, A., Giusa, D., and Augello, R., "Nonlinear analysis of thin-walled beams with highly deformable sections," *International Journal of Non-Linear Mechanics*, Vol. 128, January 2021. https://doi.org/10.1016/j.ijnonlinmec.2020.103613.

[36] Augello, R., and Carrera, E., "Nonlinear dynamics and band gap evolution of thin-walled metamaterial-like structures," *Journal of Sound and Vibration*, Vol. 578, 26 May 2024. https://doi.org/10.1016/j.jsv.2024.118329.

List of Tables

List of Figures